Research Square

Preprints are preliminary reports that have not undergone peer review.
They should not be considered conclusive, used to inform clinical practice,
or referenced by the media as validated information.

ATS-Flood: An Automated Time-Series SAR Framework for Flood Mapping Using Pixel-Wise Statistical Change Analysis

Hadi Farhadi
K.N Toosi University of Technology
Hamid Ebadi
ebadi@kntu.ac.ir

K.N Toosi University of Technology
Abbas Kiani
Babol Noshirvani University of Technology

Research Article

Keywords: Sentinel-1 SAR, Multi-temporal analysis, Flood Mapping, Automated Flood Detection, Disaster monitoring

Posted Date: November 26th, 2026

DOI: https://doi.org/10.21203/rs.3.rs-11515210/v1

License: This work is licensed under a Creative Commons Attribution 4.0 International License.
Read Full License

Additional Declarations: No competing interests reported.

ATS-Flood: An Automated Time-Series SAR Framework for Flood Mapping Using Pixel-Wise Statistical Change Analysis

Hadi Farhadi[1], Hamid Ebadi [2*], Abbas Kiani [3]

1- Faculty of Geodesy and Geomatics Engineering, K.N Toosi University of Technology, Tehran, Iran; Hadi.farhadiabeshahmadloo@email.kntu.ac.ir

2*- Faculty of Geodesy and Geomatics Engineering, K.N Toosi University of Technology, Tehran, Iran; ebadi@kntu.ac.ir

3- Faculty of Civil Engineering, Babol Noshirvani University of Technology, Babol, Iran; a.kiani@nit.ac.ir

Abstract

Rapid and accurate flood mapping is essential for emergency response, disaster management, and post-event damage assessment. Synthetic Aperture Radar (SAR) imagery has become one of the most reliable data sources for flood monitoring because of its all-weather and day-and-night imaging capabilities. However, existing SAR-based flood mapping approaches often suffer from scene-dependent threshold selection, temporal backscatter variability, speckle effect, and false detections caused by soil moisture, permanent water bodies, and complex land-cover conditions. To address these challenges, this study proposes a fully automatic flood detection framework, referred to as ATS-Flood, based on multi-temporal Sentinel-1 SAR observations. The proposed framework first characterizes the normal backscatter behavior of each pixel using pre-flood time-series images and then detects flood-induced changes through a standardized change metric. Otsu thresholding algorithm is employed to automatically determine the optimal decision threshold, while complementary VV and VH polarizations are integrated to enhance flood detection reliability. In addition, permanent-water and terrain-slope masks are incorporated to reduce commission errors, and the detected flooded areas are further categorized into Strong Flood Signal (SFS) and Weak Flood Signal (WFS) classes to provide a more informative representation of flood extent. The framework was evaluated using the 2019 Khuzestan flood event in southwestern Iran and validated against Copernicus Emergency Management Service (EMS) reference maps, Sentinel-2 imagery, and high-resolution optical observations. Experimental results demonstrate that the proposed method achieved an Overall Accuracy of 93.25%, a Kappa Coefficient of 0.865, and F1-scores exceeding 93%, outperforming eight

widely used benchmark methods, including S1-VV, S1-VH, SDWI, NDFI-VV, NDFI-VH, UN-VV, UN-VH, and SBFD. Sensitivity analyses further confirmed the robustness of the automatic thresholding strategy and the effectiveness of combining ascending and descending Sentinel-1 acquisitions. These results demonstrate that ATS-Flood provides an accurate, robust, and fully automated solution for large-scale operational flood mapping using SAR imagery.

Keywords: Sentinel-1 SAR, Multi-temporal analysis, Flood Mapping, Automated Flood Detection, Disaster monitoring.

1. Introduction

Floods are among the most devastating natural hazards, occurring annually in many regions of the world and causing substantial losses to human lives, infrastructure, natural resources, and economic activities (Blaikie et al., 2014). Owing to their highly dynamic nature and rapid spatial expansion, flood events can inundate extensive areas within a short period, resulting in severe and often irreversible socioeconomic and environmental consequences (Change, 2001; Tellman et al., 2021). In particular, riverine floods are recognized as one of the primary drivers of damage to agricultural lands, urban areas, transportation networks, and other land-use classes, with long-term impacts on regional development and the livelihoods of affected communities (Tellman et al., 2021).

Consequently, the rapid and accurate delineation of flood extent is a fundamental prerequisite for effective emergency response, disaster management, damage assessment, and post-event decision-making (Schumann, G. J.-P. & Moller, 2015). Beyond emergency response, accurate flood extent maps constitute an essential source of information for hydrological and hydraulic studies (Farhadi & Najafzadeh, 2021). They provide valuable inputs for flood hazard assessment , calibration and validation of hydrological and hydraulic models, estimation of flood frequency and inundation dynamics, and the development of early warning systems (Mosalla Tabari et al., 2025). Therefore, improving the accuracy and reliability of flood mapping is important not only for remote sensing applications but also for advancing flood-risk analysis and water resources management. However, conventional field-based flood surveys are often impractical because of the large spatial extent of inundated areas, hazardous environmental conditions, limited accessibility, and the rapidly evolving nature of flood events (Schumann, G. J. et al., 2018). In this context, remote sensing has emerged as an indispensable tool for flood monitoring and mapping by providing extensive, repetitive, and multi-temporal observations that enable timely and large-scale assessment of flood-affected areas (Farhadi et al., 2025b).

Various remote sensing data sources, including optical imagery (Farhadi et al., 2024a), Synthetic Aperture Radar (SAR) data (Dodangeh et al., 2021), and Unmanned Aerial Vehicle (UAV) (Barkhade et al., 2023) observations, have been extensively employed for flood detection and monitoring. Optical imagery provides rich spectral information in the visible, Near-Infrared (NIR), and Shortwave Infrared (SWIR) regions, enabling effective discrimination between water bodies and other land-cover types (Bayati & Danesh-Yazdi, 2021). Accordingly, numerous spectral water indices, such as Normalized Difference Water Index (NDWI) (Gao, 1996; McFeeters, 1996), Modified Normalized Difference Water Index (MNDWI) (Xu, 2006), Automated Water Extraction Index (AWEI) (Feyisa et al., 2014), Flood Water Extraction Index (FWEI) (Farhadi et al., 2024b), and Sentinel-2 Flood Monitoring Index (SFMI) (Farhadi et al., 2025a), have been developed to facilitate flood mapping from optical data. Despite these advantages, the applicability of optical imagery is fundamentally constrained by atmospheric conditions and solar illumination. Because flood events frequently coincide with intense rainfall and extensive cloud cover, acquiring cloud-free optical images during the critical stages of flooding is often challenging. Nevertheless, when inundation persists for an extended period, optical imagery remains a valuable source of information for delineating flood extent (Farhadi et al., 2022).

In contrast, UAV imagery offers ultra-high spatial resolution, enabling detailed observation of flood-affected areas and the acquisition of high-quality reference data for validation and damage assessment (Barkhade et al., 2023). However, its operational use in large-scale flood monitoring is constrained by limited spatial coverage, the need for field deployment, dependence on weather and flight conditions, relatively high operational costs, and the impracticality of repeated acquisitions over extensive regions (Colomina & Molina, 2014; Giordan et al., 2018). These limitations considerably restrict the applicability of UAV-based observations for rapid and regional-scale flood mapping.

In contrast, Synthetic Aperture Radar (SAR) imagery has become one of the most reliable data sources for operational flood monitoring due to its ability to acquire observations independently of weather conditions and solar illumination (Martinis et al., 2009; Schlaffer et al., 2015; Landuyt et al., 2018; Ezzine et al., 2020; Mohsenifar et al., 2025). By operating in the microwave region of the electromagnetic spectrum, SAR sensors can penetrate cloud cover and provide day-and-night imaging capabilities, making them particularly suitable for monitoring flood events that frequently occur under adverse weather conditions. Furthermore, the wide spatial coverage, short revisit intervals, and free availability of Sentinel-1 SAR data have significantly enhanced the use of radar imagery in near-real-time flood monitoring and emergency response applications (Farhadi et al., 2025b). Open water surfaces typically exhibit very low SAR backscatter as a result of specular reflection, allowing

inundated areas to be effectively distinguished from many non-water land-cover types. Nevertheless, accurate flood delineation from SAR imagery remains a challenging task. The presence of inherent speckle effect, together with backscatter variability induced by surface roughness (Pulvirenti et al., 2011), soil moisture, land-cover characteristics (Twele et al., 2016), topographic effects, and imaging geometry, may produce SAR responses similar to those of flooded areas, thereby increasing the likelihood of misclassification (Martinis et al., 2015; Schumann, G. J.-P. et al., 2015). Consequently, developing robust and reliable approaches that fully exploit the capabilities of SAR data for accurate flood mapping continues to be an active area of research.

Early approaches for flood delineation from SAR imagery were predominantly based on thresholding techniques (Chini et al., 2017; Moharrami et al., 2021). For example, Martinis et al. (2009) proposed an automatic split-based thresholding procedure for near-real-time flood mapping from TerraSAR-X imagery, while Chini et al. (2017) introduced a hierarchical thresholding strategy to improve threshold selection over heterogeneous landscapes. Although these methods enhanced the automation of flood extraction, their performance remained strongly influenced by scene-dependent backscatter variability and threshold selection (Li, Z. et al., 2025). These methods exploit the contrast in SAR backscatter between open water and surrounding non-water surfaces by defining a threshold value (Liang & Liu, 2020), whereby pixels with backscatter values below the specified threshold are classified as flooded areas (Moharrami et al., 2021). Owing to their conceptual simplicity, computational efficiency, and independence from training data, threshold-based methods have been widely adopted in both research studies and operational flood mapping systems (Martinis et al., 2009). However, their performance is highly sensitive to threshold selection (Chini et al., 2017). SAR backscatter is influenced not only by the presence of surface water but also by a range of environmental and imaging factors, including land-cover characteristics, soil moisture, surface roughness, incidence angle, and topographic conditions (Twele et al., 2016). Consequently, applying a single fixed threshold—particularly to raw VV and VH backscatter coefficients, often fails to provide consistent performance across heterogeneous landscapes (Farhadi et al., 2025b). Moreover, natural backscatter variations associated with agricultural fields, vegetated areas, Arid regions (Garg et al., 2025) and structurally complex surfaces may exhibit signatures similar to those of inundated regions, leading to increased commission and omission errors (Bioresita et al., 2018). These limitations, particularly the dependence of threshold-based methods on the spatial and temporal variability of SAR backscatter, have motivated the development of more advanced approaches based on change detection, time-series analysis, and data-driven techniques.

To overcome the limitations of conventional thresholding approaches, change detection techniques have been widely adopted for SAR-based flood mapping (Hotaki, S. et al., 2025; Hotaki, S. F. et al., 2026). Several change detection strategies have been proposed to enhance flood mapping by exploiting temporal SAR observations. For instance, Li et al. (2018) developed an automatic bi-temporal change detection framework for Sentinel-1 imagery, whereas Schlaffer et al. (2015) combined harmonic time-series analysis with change detection to better characterize seasonal backscatter variations. More recently, Mohsenifar et al. (2025) introduced a wavelet-based flood-change index to improve rural flood mapping from bi-temporal Sentinel-1 data. These methods typically identify inundated areas by comparing pre-event and post-event SAR observations and interpreting significant backscatter variations as indicators of flooding (Cian et al., 2018; Dixit & Chawla, 2026). Compared with single-image thresholding methods, change detection approaches are generally more robust to spatial heterogeneity because they emphasize temporal changes rather than absolute backscatter values (Li, Y. et al., 2018). Nevertheless, their performance remains highly dependent on the selection of suitable reference images and acquisition timing (Risling et al., 2024). Seasonal land-cover dynamics, vegetation phenology, agricultural activities, and soil moisture fluctuations can all induce backscatter variations similar to those caused by flooding, making it challenging to distinguish flood-induced changes from natural environmental variability (Hotaki, S. F. et al., 2026).

With the increasing availability of Earth Observation (EO) data and advances in Artificial Intelligence, Machine Learning (ML) algorithms, including Random Forest (RF) (Billah et al., 2023), Support Vector Machine (SVM) (Gašparović & Klobučar, 2021), and Decision Tree (DT) (Amos et al., 2026), have been extensively applied to flood mapping. By integrating spectral, spatial, topographic, and SAR-derived features, these algorithms are capable of modeling complex nonlinear relationships between input variables and land-cover classes, often outperforming conventional rule-based approaches (Bereczky et al., 2022). Despite their promising performance, ML-based methods are highly dependent on the availability of large and representative training datasets (Hosseiny et al., 2019). Preparing reliable labeled samples, particularly for large-scale or long-duration flood events, is often labor-intensive, time-consuming, and costly (Lan & Wang, 2025). Moreover, trained models frequently exhibit limited transferability to new geographic regions and may require recalibration or retraining when applied under different environmental conditions (Amos et al., 2026).

More recently, Deep Learning (DL) techniques have attracted considerable attention for flood mapping because of their ability to automatically learn hierarchical spatial features directly from remotely sensed imagery (Banerjee & Daou, 2026; Ebrahimi et al., 2026). Deep neural network architectures, such as Convolutional Neural

Networks (CNNs) (Seydi et al., 2022), U-Net (Ebrahimi et al., 2026), and their variants, have demonstrated remarkable performance in distinguishing flooded areas from other land-cover classes. However, their operational implementation remains constrained by several challenges, including the requirement for large volumes of labeled training data, substantial computational resources, long training times, and limited generalization across diverse geographic environments (Kaçmaz & Alganci, 2026). Furthermore, the black-box nature of many deep learning models restricts their interpretability, providing limited insight into the underlying decision-making process (Yu et al., 2026). In addition, a large proportion of existing ML- and DL-based studies rely primarily on single-date imagery or a limited number of observations, thereby failing to fully exploit the rich temporal information available in SAR time series (Li, S. et al., 2026).

Although time-series SAR approaches have been increasingly explored in recent years, many existing methods still rely on pairwise image comparisons or empirically defined criteria to identify flood-induced changes (Moharrami et al., 2021). Nevertheless, most existing time-series approaches still characterize temporal variation through image-to-image comparisons or scene-level statistical descriptors rather than explicitly modeling the historical behavior of individual pixels. However, each pixel in a SAR image exhibits a unique temporal backscatter behavior governed by the relatively stable and dynamic environmental characteristics of its location (Farhadi et al., 2025b). Characterizing this temporal behavior as a statistical reference provides an opportunity to identify anomalous backscatter variations associated with flooding more reliably than methods based solely on absolute backscatter values or pairwise image comparisons . Furthermore, while ML- and DL-based methods are effective at capturing complex data patterns, their performance often depends on extensive training datasets and features extracted from a limited number of observations (Garg et al., 2025). In contrast, exploiting the intrinsic temporal behavior of individual pixels enables the detection of flood-induced anomalies without requiring large training datasets, while simultaneously reducing dependence on empirically selected thresholds. Therefore, developing frameworks that analyze the statistical temporal behavior of each pixel relative to its historical reference has the potential to improve the robustness, interpretability, and transferability of SAR-based flood mapping methods.

Motivated by these challenges, this study proposes an automated framework for flood mapping based on Sentinel-1 SAR time-series observations. Unlike conventional approaches that primarily rely on absolute backscatter values, fixed thresholds, or data-driven models requiring extensive training data, the proposed framework characterizes the temporal behavior of each pixel relative to its historical reference and identifies flood events through pixel-wise statistical change analysis. By accounting for the inherent temporal variability of radar

backscatter, the proposed approach mitigates the influence of land-cover heterogeneity, natural backscatter fluctuations, and empirically defined thresholds, thereby enabling more robust and automated flood delineation. The main contributions of this study are summarized as follows:

- An automated Sentinel-1 SAR time-series framework (ATS-Flood) is developed for robust and efficient flood extent delineation.
- A pixel-wise statistical change analysis approach is proposed, in which the temporal behavior of each pixel is characterized relative to its historical reference, improving robustness against land-cover heterogeneity and environmentally induced backscatter variability.
- An interpretable and training-data-independent framework is introduced, reducing reliance on extensive labeled datasets and empirically selected thresholds while maintaining high applicability for operational flood mapping.
- The proposed framework is comprehensively evaluated over a large and geographically complex flood-prone region using independent reference datasets and standard quantitative accuracy metrics.

Therefore, the objective of this study is not only to improve the accuracy and robustness of SAR-based flood mapping but also to develop a practical and transferable framework that can be integrated into large-scale operational flood monitoring systems. Owing to its fully automatic workflow and reliance on freely available Sentinel-1 imagery, the proposed framework has the potential to support disaster management authorities, early-response operations, hydrological monitoring, and evidence-based decision-making during flood events. Moreover, the generated flood maps can serve as reliable inputs for hydrological and hydraulic modeling, flood hazard assessment, and operational flood forecasting systems, thereby supporting evidence-based water resources and disaster management.

2. Study Area and EO Data

2.1. Study Areas

The study was conducted over Khuzestan Province, located in southwestern Iran between approximately 30°–33° N latitude and 47°–50° E longitude (Figure 1). Covering an area of about 64,000 km², Khuzestan is one of the most flood-prone regions in Iran owing to its extensive low-relief alluvial plains, dense river network, and downstream location within several major river basins. The province contains the country's largest surface water system, including the Karun, Karkheh, Dez, Marun, and Jarahi rivers, which convey runoff from the mountainous catchments of the Zagros Mountains toward the Persian Gulf. Because Khuzestan is situated at the outlet of these upstream basins, heavy rainfall over the Zagros region can rapidly increase river discharge and generate

widespread inundation across the downstream floodplains. Most of the province consists of flat terrain with very gentle slopes, which considerably reduces drainage efficiency and promotes the formation of extensive floodwater inundation during high-flow events. Consequently, large agricultural lands, urban areas, and wetlands are highly vulnerable to riverine flooding.

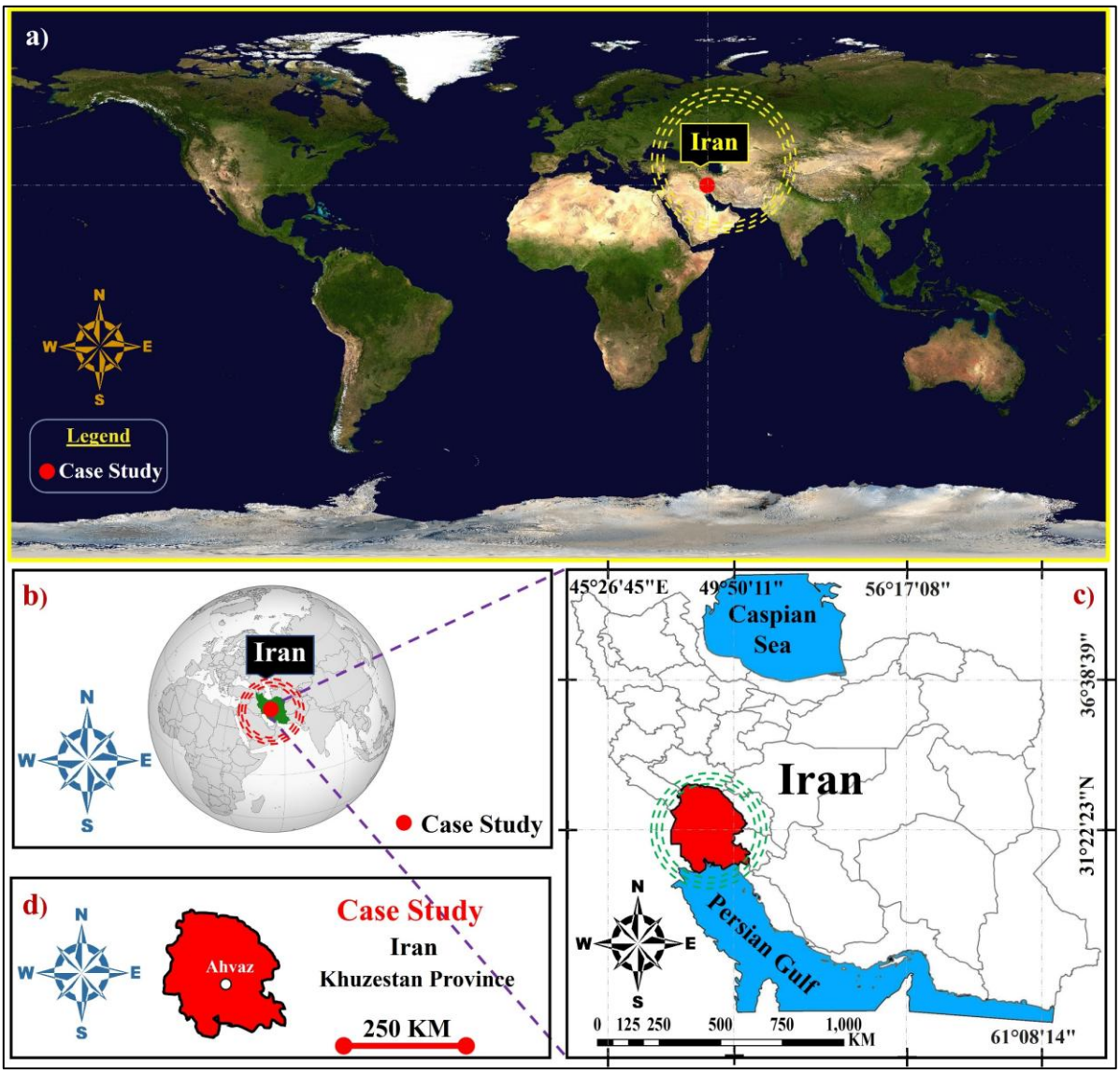


Figure 1. Geographic location of the study area. (a) Global view showing the location of Iran. (b) Regional view highlighting Iran within the Middle East. (c) Location of Khuzestan Province in southwestern Iran. (d) Boundary of the study area used in this research.

The study focuses on the March–April 2019 flood event, one of the most severe floods recorded in Iran in recent decades. Triggered by persistent extreme precipitation over the upstream catchments, together with high reservoir inflows and controlled dam releases, the event inundated large parts of Khuzestan, causing extensive damage to agricultural areas, infrastructure, and residential settlements. Owing to its large spatial extent, diverse land-cover types, complex hydrological conditions, and availability of multi-temporal Sentinel-1 observations,

Khuzestan provides an ideal test site for evaluating the robustness and applicability of the proposed time-series SAR flood mapping framework.

2.2. EO Data and Pre-Processing

Multiple datasets were used in this study to develop, implement, and validate the proposed framework. The characteristics, sources, and preprocessing details of these datasets are presented in the following subsections.

2.2.1. Sentinel-1 SAR Data and Preprocessing

Sentinel-1 Ground Range Detected (GRD) products available in the Google Earth Engine (GEE) platform were used as the primary data source for flood mapping. The post-flood Sentinel-1 acquisition used in this study was acquired on 8 March 2019, whereas the reference dataset was constructed from the pixel-wise mean backscatter derived from all available Sentinel-1 acquisitions during the one-month period preceding the flood event. This reference period was selected to characterize the normal pre-flood backscatter behavior of each pixel while minimizing the influence of short-term fluctuations and providing a reliable baseline for subsequent statistical change analysis. Before being made available to users, the Sentinel-1 GRD archive in GEE undergoes a series of standard preprocessing procedures implemented by the European Space Agency (ESA). These include radiometric calibration to convert the raw SAR measurements into sigma naught (σ^0) backscatter coefficients, thermal noise removal, terrain correction, and geometric correction to ensure accurate geolocation. As a result, the imagery is provided in a radiometrically and geometrically consistent form suitable for time-series analysis. Unlike the aforementioned preprocessing steps, speckle filtering is not applied by default within the Sentinel-1 collection in GEE. Therefore, to reduce speckle effect while preserving image details, the Refined Lee (Lee et al., 2008) filter was applied to all SAR observations. Additional preprocessing operations were subsequently performed, including spatial clipping based on the study area boundary and temporal filtering to select the SAR acquisitions corresponding to the analysis period. The Sentinel-1 GRD products provide dual-polarization observations (VV and VH) with a spatial resolution of 10 m. To maximize temporal coverage and improve flood detection capability, both Ascending and Descending orbit acquisitions with VV and VH polarizations were incorporated into the proposed time-series framework.

Figure 2 presents the pre-flood Sentinel-1 SAR imagery used as the reference dataset in this study. The figure includes the mean VV and VH backscatter images, as well as the VV/VH ratio, computed from all Sentinel-1 acquisitions collected during the one month prior to the March 8, 2019 flood event. Averaging the pre-flood observations reduces the influence of short-term backscatter fluctuations and provides a representative baseline for subsequent statistical change analysis.

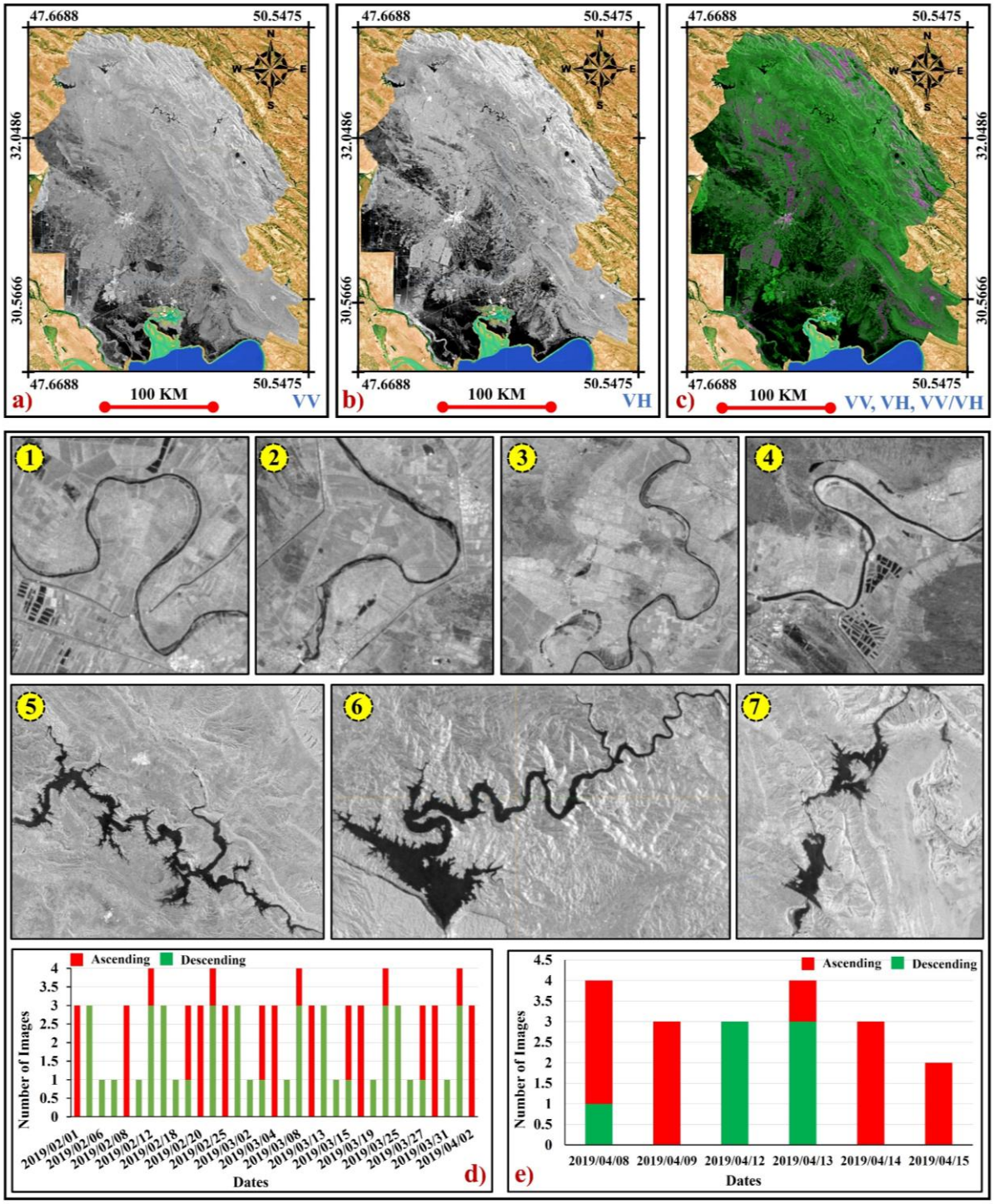


Figure 2. Mean Sentinel-1 SAR image representing the one-month pre-flood period: a) VV backscatter, b) VH backscatter, c) false-color composite of VV, VH, and VV/VH ratio, d) Pre-Flood Sentinel-1 SAR Data Availability and e) Post-Flood Sentinel-1 SAR Data Availability. The labels 1–4 indicate rivers and narrow water bodies, whereas labels 5–7 denote reservoirs, as observed in the Sentinel-1 VV polarization image.

2.2.2. Digital Elevation Model (DEM) data

In this study, the Shuttle Radar Topography Mission (SRTM) Digital Elevation Model (DEM) was used as the primary source of topographic information. The SRTM DEM was generated from Radar observations acquired by the Space Shuttle Endeavour during the Shuttle Radar Topography Mission in 2000 and provides near-global

elevation coverage at a spatial resolution of approximately 30 m. The dataset is freely available through several platforms, including GEE, and enables the derivation of topographic variables such as elevation, slope, and aspect. In this study, the SRTM DEM was utilized to characterize terrain conditions, improve the identification of low-lying and flood-prone areas, and enhance the accuracy of flood mapping. Since the SRTM dataset is provided in a georeferenced and analysis-ready format within GEE, no additional preprocessing was required except for clipping the DEM to the boundary of the study area.

2.2.3. JRC Global Surface Water

To distinguish permanent water bodies from flood-induced inundation, the JRC Global Surface Water (GSW) dataset developed by the European Commission Joint Research Centre (JRC) was employed in this study. The dataset is readily available within the GEE platform and can be directly integrated into geospatial analyses. It was generated through long-term analysis of the Landsat satellite archive, spanning more than three decades (1984 to the present), and is widely recognized as one of the most comprehensive global datasets for monitoring surface water dynamics (Pekel et al., 2016). For each pixel, the historical presence or absence of surface water is analyzed over the entire observation period, from which a suite of statistical indicators describing the temporal dynamics of surface water is derived. Among the available layers, the Occurrence product was used in this study to identify permanent water bodies. This layer represents the percentage of observations in which water was detected for each pixel throughout the entire observation period, with values ranging from 0% to 100%. Pixels with high occurrence values were considered permanent water bodies and were excluded from the detected flood extent.

2.2.3. Validation Data

The performance of the proposed flood mapping framework was evaluated using authoritative reference datasets. The primary reference data were obtained from the Copernicus Emergency Management Service (EMS), which provides high-resolution rapid mapping products for natural disasters, including floods, wildfires, and earthquakes. The flood extent maps are generated from very high-resolution satellite imagery and validated by expert analysts, making them a reliable benchmark for flood mapping accuracy assessment. For the 2019 Khuzestan flood event, the Copernicus EMS activation EMSR352 provides detailed reference flood maps for multiple affected areas across the province. These datasets have been widely adopted as reference data for validating flood mapping methods in previous studies (Farhadi et al., 2024b; Farhadi et al., 2025b). Therefore, they were employed in this study as the primary ground reference for quantitative accuracy assessment. Overall, twelve flood-affected regions documented by Copernicus EMS were used for validation in this study. The characteristics of the reference datasets, including the mapped regions, image sources, and acquisition dates, are

summarized in Figure 3. To further support the visual interpretation of flood extent, Sentinel-2 optical imagery (10 m spatial resolution) and high-resolution Google Earth imagery were also utilized as auxiliary datasets. These complementary data facilitate the interpretation of land-cover characteristics and flood boundaries, particularly in areas where independent visual verification is required.

3. Methodology

The proposed Automated Time-Series SAR Framework for Flood Mapping Using Pixel-Wise Statistical Change Analysis (ATS-Flood) is developed based on Sentinel-1 SAR time-series observations. Owing to its capability for all-weather, day-and-night imaging, SAR provides a reliable data source for flood monitoring, particularly during extreme weather conditions when optical observations are often unavailable.

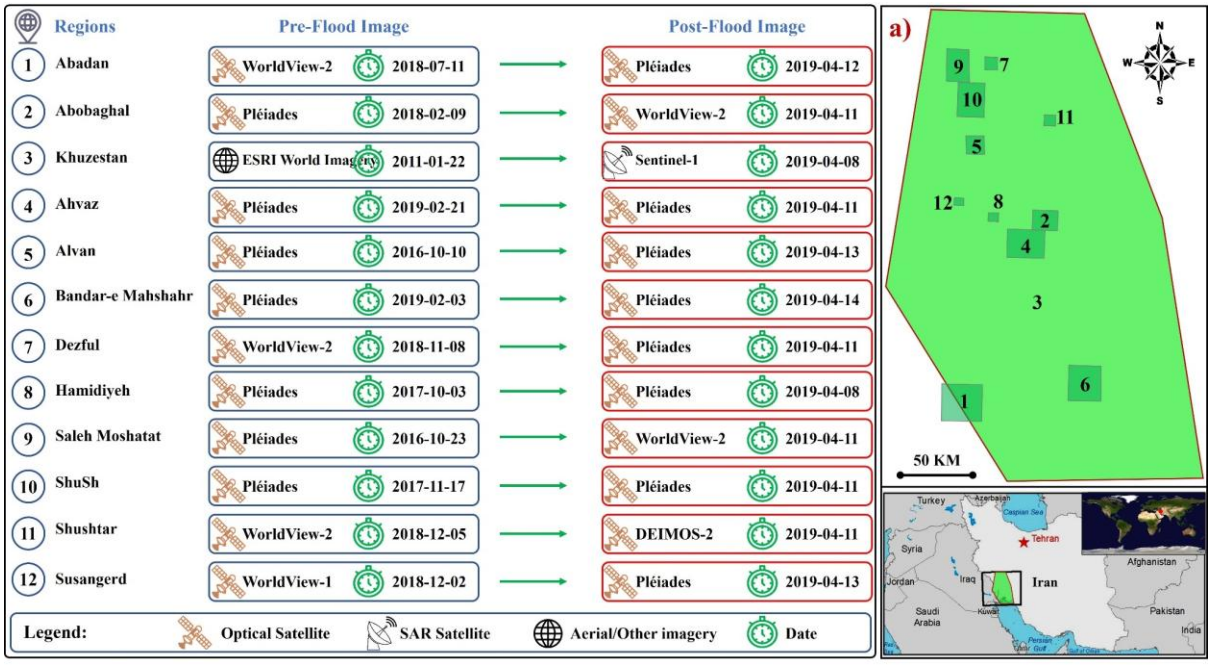


Figure 3. Characteristics of the EMS reference datasets, including the mapped regions (a: Locations), image sources, and acquisition dates.

The overall workflow of the proposed methodology is illustrated in Figure 4. The proposed framework consists of four main stages: (1) data acquisition in the GEE platform, (2) data preprocessing, (3) flood mapping through the proposed processing workflow, and (4) accuracy assessment. Each stage is described in detail in the following subsections.

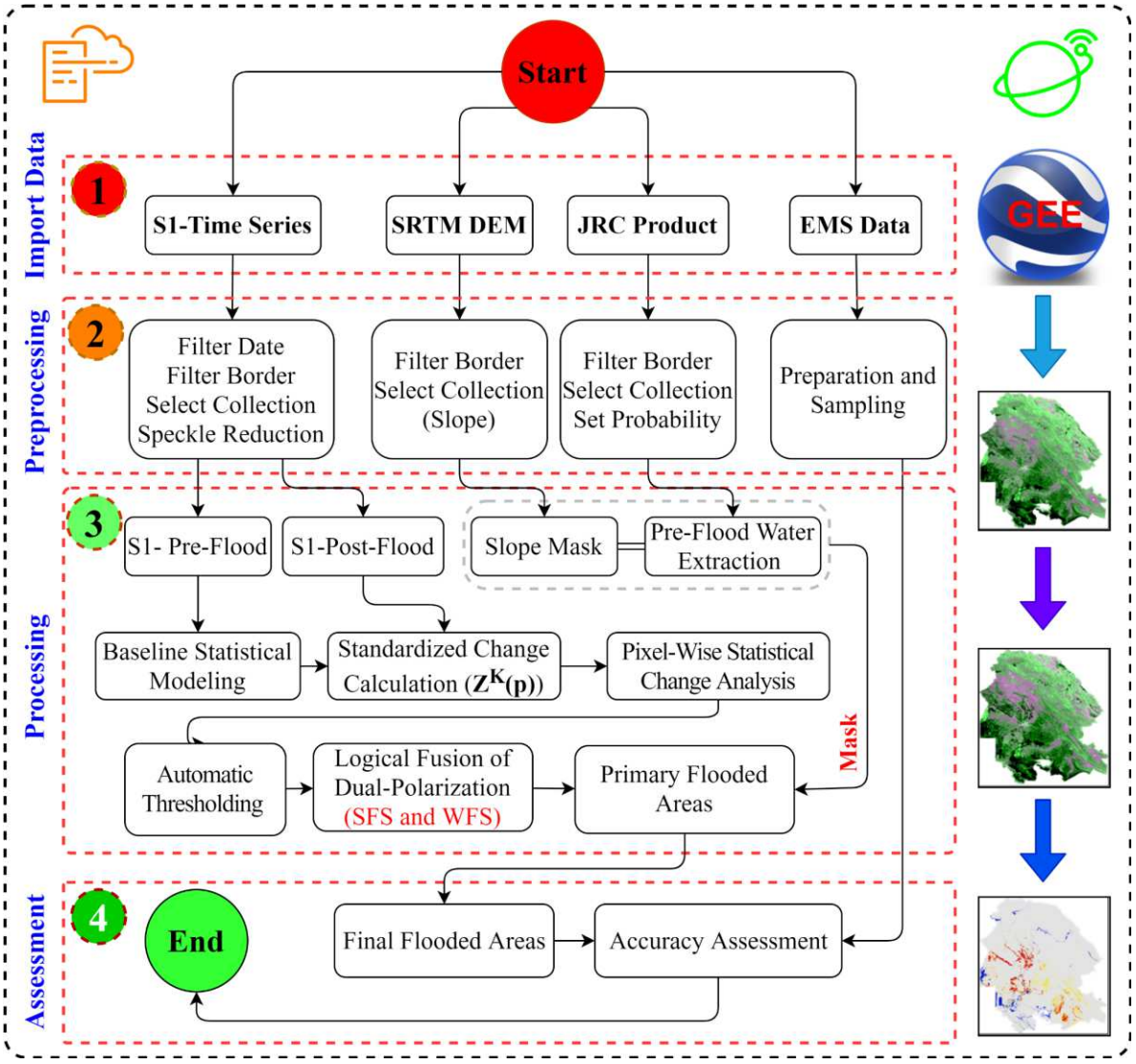


Figure 4. Overall architecture of the proposed ATS-Flood framework, including Sentinel-1 SAR preprocessing, historical reference generation, pixel-wise statistical change analysis, flood candidate extraction, and Accuracy Assessment.

3.1. Background of the Proposed Flood Detection Algorithm

Flood events are characterized by the rapid expansion of surface water into areas that are normally dry. In SAR imagery, open water surfaces typically exhibit very low Radar backscatter because specular reflection dominates the scattering mechanism, causing most of the incident microwave energy to be reflected away from the sensor. Consequently, the returned backscatter signal (σ^0) from inundated areas is generally much lower than that of most terrestrial land-cover types. This characteristic has formed the physical basis of numerous SAR-based flood mapping approaches. Despite this favorable scattering behavior, the direct use of SAR backscatter intensity for flood detection remains challenging. Radar backscatter is influenced not only by the presence of surface water but also by multiple environmental and imaging factors, including land-cover characteristics, surface roughness,

soil moisture, vegetation structure, speckle effect, topographic conditions, and sensor acquisition geometry. As a result, similar backscatter values may correspond to different surface conditions, making it difficult to define a universal threshold that can be reliably applied across different regions and acquisition dates.

To address these limitations, the proposed ATS-Flood framework adopts a pixel-wise statistical change analysis strategy that evaluates the temporal behavior of each pixel relative to its own historical reference. Instead of relying on absolute backscatter values or globally defined thresholds, the proposed approach identifies flood-induced anomalies by quantifying the statistical deviation of each pixel from its normal temporal behavior. By using the intrinsic temporal characteristics of individual pixels as the reference, the framework effectively accounts for local environmental variability and spatial heterogeneity, thereby improving the robustness, stability, and transferability of flood mapping results while reducing dependence on empirically selected thresholds. The detailed methodology of the proposed algorithm is presented in the following subsections.

3.1.1. Construction of the Historical Pixel-Wise Reference

The first stage of the proposed ATS-Flood framework is the construction of a historical reference representing the normal backscatter behavior of each pixel under non-flood conditions. To this end, a time series of Sentinel-1 SAR images acquired prior to the flood event is selected as the reference dataset. In the present study, the reference period consists of Sentinel-1 observations acquired during the one-month period preceding the flood event. More generally, the reference period should correspond to flood-free conditions and is selected based on available hydrometeorological information and historical flood records for the study area.

For each pixel p and each SAR polarization $k \in \{VV, VH\}$, two fundamental statistical descriptors are computed from the reference time series: the temporal mean and the temporal standard deviation of the backscatter coefficient. These statistics characterize the normal temporal behavior of each pixel and provide a pixel-specific baseline against which flood-induced anomalies are evaluated in subsequent processing steps. By constructing an independent statistical reference for every pixel, the proposed framework accounts for local environmental characteristics and reduces the influence of spatial heterogeneity on flood detection. The temporal mean backscatter coefficient is computed as follows:

$$m_{pre}^{(k)}(p) = \frac{1}{N} \sum_{i=1}^{N} I_{i,pre}^{(k)}(p) \tag{1}$$

where N denotes the number of Sentinel-1 SAR images acquired during the pre-flood reference period, and $\sum_{i=1}^{N} I_{i,pre}^{(k)}(p)$ represents the SAR backscatter coefficient of pixel p in the *i-th* image for polarization k. The

resulting temporal mean, characterizes the expected backscatter behavior of each pixel under normal (non-flood) conditions and serves as the historical reference for detecting flood-induced anomalies in the subsequent stages of the proposed framework. The corresponding temporal standard deviation is computed as follows:

$$\sigma_{pre}^{(k)}(p)=\sqrt{\frac{1}{N-1}\sum_{i=1}^{N}\left(I_{i,pre}^{(k)}(p)-\mu_{pre}^{(k)}(p)\right)^2} \tag{2}$$

The temporal standard deviation quantifies the natural variability of SAR backscatter for each pixel during the reference period. By accounting for this variability, the proposed framework evaluates flood-induced changes relative to the normal behavior of individual pixels rather than relying solely on absolute backscatter differences. This normalization suppresses false detections in areas with inherently high temporal variability and enhances the stability of flood mapping across heterogeneous landscapes. More importantly, this step constitutes the core innovation of the proposed ATS-Flood framework by establishing a pixel-specific historical reference, allowing flood detection to be based on statistically significant deviations from normal temporal behavior rather than absolute SAR backscatter values.

3.1.2. Standardized Post-Event Change Analysis

After establishing the historical backscatter reference, the post-flood SAR observation is compared with the reference statistics for each pixel. Specifically, the standardized backscatter change is computed for each pixel p and polarization k according to Equation (3):

$$Z^{(k)}(p)=\frac{I_{post}^{(k)}(p)-\mu_{pre}^{(k)}(p)}{\sigma_{pre}^{(k)}(p)} \tag{3}$$

where $I_{post}^{(k)}(p)$ denotes the post-flood SAR backscatter of pixel p, while $\mu_{pre}^{(k)}(p)$ and $\sigma_{pre}^{(k)}(p)$ represent the temporal mean and temporal standard deviation of the same pixel during the reference period, respectively. This standardized metric ($Z^{(K)}(P)$) quantifies the deviation of the post-event observation from the historical behavior of each pixel in units of standard deviation. Consequently, the observed change is normalized according to the intrinsic temporal variability of each pixel, allowing consistent comparison across heterogeneous land-cover types. Since flood inundation generally leads to a reduction in SAR backscatter due to specular reflection from open water surfaces, large negative Z values indicate a higher likelihood of flooding. However, to quantify the magnitude of deviation irrespective of its direction, the absolute standardized change is computed as:

$$\Delta^{(k)}(p)=\left|Z^{(k)}(p)\right| \tag{4}$$

3.1.3. Automatic Decision Thresholding

Following the computation of the Standardized Change Metric (SCM, $\Delta^K(P)$), an optimal decision threshold is automatically determined to separate flooded from non-flooded pixels. Unlike conventional approaches that rely on empirically selected or trial-and-error thresholds, the proposed framework employs the Otsu algorithm to derive the threshold directly from the statistical distribution of the standardized change values (Otsu, 1979). The optimal threshold is obtained by maximizing the between-class variance, as expressed in Equation (5).

$$t^* = \arg\max_t \left[\omega_1(t)\omega_2(t)\left(\mu_1(t) - \mu_2(t)\right)^2 \right] \tag{5}$$

In Equation (5), t^* denotes the optimal threshold, $\omega 1(t)$ and $\omega 2(t)$ represent the probabilities of the two classes at threshold t, and $\mu 1(t)$ and $\mu 2(t)$ correspond to the mean Standardized Change Values (SCV) of the respective classes. By maximizing the between-class variance, the algorithm identifies the threshold that provides the greatest statistical separability between flooded and non-flooded pixels. Because the SCVs are normalized with respect to the historical behavior of each pixel, their statistical distribution is considerably more consistent than that of the original SAR backscatter values. Consequently, the proposed framework can determine the decision threshold in a fully automatic and data-driven manner, eliminating the need for empirically tuned parameters while improving the robustness and transferability of flood extraction across different flood events and geographic regions. The thresholding procedure is performed independently for the VV and VH polarizations according to Equation (6) and Equation (7), respectively.

$$t_{VV} = Otsu\left(\Delta^{(VV)}\right) \tag{6}$$

$$t_{VH} = Otsu\left(\Delta^{(VH)}\right) \tag{7}$$

This step eliminates the dependence on manually selected thresholds, improving the automation, repeatability, and operational applicability of the proposed framework across different flood events and study areas.

3.1.4. Logical fusion of dual-polarization

To improve the reliability of flood detection and reduce classification uncertainty, the binary flood maps derived independently from the VV and VH polarizations were logically combined. The proposed framework employs an automatic thresholding strategy based on the Otsu algorithm together with a dual-confidence flood classification scheme, distinguishing between Strong Flood Signal (SFS) and Weak Flood Signal (WFS). This strategy exploits the complementary scattering characteristics of the two SAR polarizations, allowing flood candidates to be categorized according to the consistency of their responses. Pixels exhibiting a strong flood signature in both polarizations are classified as SFS, whereas pixels satisfying the flood criterion in only one

polarization are labeled as WFS. The SFS and WFS classes are computed using Equations (8) and (9), respectively.

$$SFS(p)=\begin{cases}1 & \Delta^{(VV)}(p)\geq t_{VV}\ \&\ \Delta^{(VH)}(p)\geq t_{VH}\\ 0 & \text{otherwise}\end{cases} \tag{8}$$

$$WFS(p)=\begin{cases}1 & \Delta^{(VV)}(p)\geq t_{VV}\ \ or\ \ \Delta^{(VH)}(p)\geq t_{VH}\\ 0 & \text{otherwise}\end{cases} \tag{9}$$

According to Equations (8) and (9), a pixel is classified as SFS when the standardized change exceeds the automatically determined threshold in both the VV and VH polarizations simultaneously. Otherwise, the pixel is assigned to the non-flood class. This conservative criterion requires consistent flood evidence from both polarizations, thereby reducing false detections and increasing the reliability of flood identification. In contrast, a pixel is classified as WFS when the threshold is exceeded in at least one of the two polarizations. Consequently, the WFS class provides a more sensitive representation of potential inundation, allowing the detection of flooded areas that may exhibit a relatively weak response in either VV or VH.

To illustrate the rationale behind this dual-polarization strategy, Figure 5 presents the distribution of SAR backscatter values for different land-cover classes in the VV and VH polarizations. As expected, all land-cover classes exhibit lower backscatter values in the VH polarization because of its stronger sensitivity to volume scattering and weaker surface returns. Permanent water bodies present the lowest backscatter in both polarizations, with values concentrated around approximately −22 dB in VV and −28 dB in VH, reflecting the dominance of specular reflection over open-water surfaces. In contrast, vegetation, agricultural lands, shrublands, and built-up areas generally exhibit higher and more variable backscatter due to surface roughness, vegetation structure, and multiple scattering mechanisms. Built-up areas show the largest variability, particularly in the VV polarization, owing to the diversity of urban structures and double-bounce scattering effects. The clear statistical separation between permanent water and the remaining land-cover classes in both polarizations demonstrates the effectiveness of combining VV and VH information for flood detection. Therefore, the proposed dual-confidence strategy provides a balanced trade-off between detection reliability and sensitivity. While the SFS class identifies inundated areas supported by strong evidence from both polarizations, the WFS class captures potential flood pixels exhibiting weaker radar signatures, thereby improving the robustness and flexibility of the proposed flood mapping framework under diverse surface conditions. Accordingly, the initial flood extent map is obtained using Equation (10), which integrates the SFS and WFS classes into a preliminary flood detection result. This step

reduces the probability of misclassification by integrating complementary information from both SAR polarizations.

$$Flood_{primary}(p) = SFS(p) \vee WFS(p) \quad (10)$$

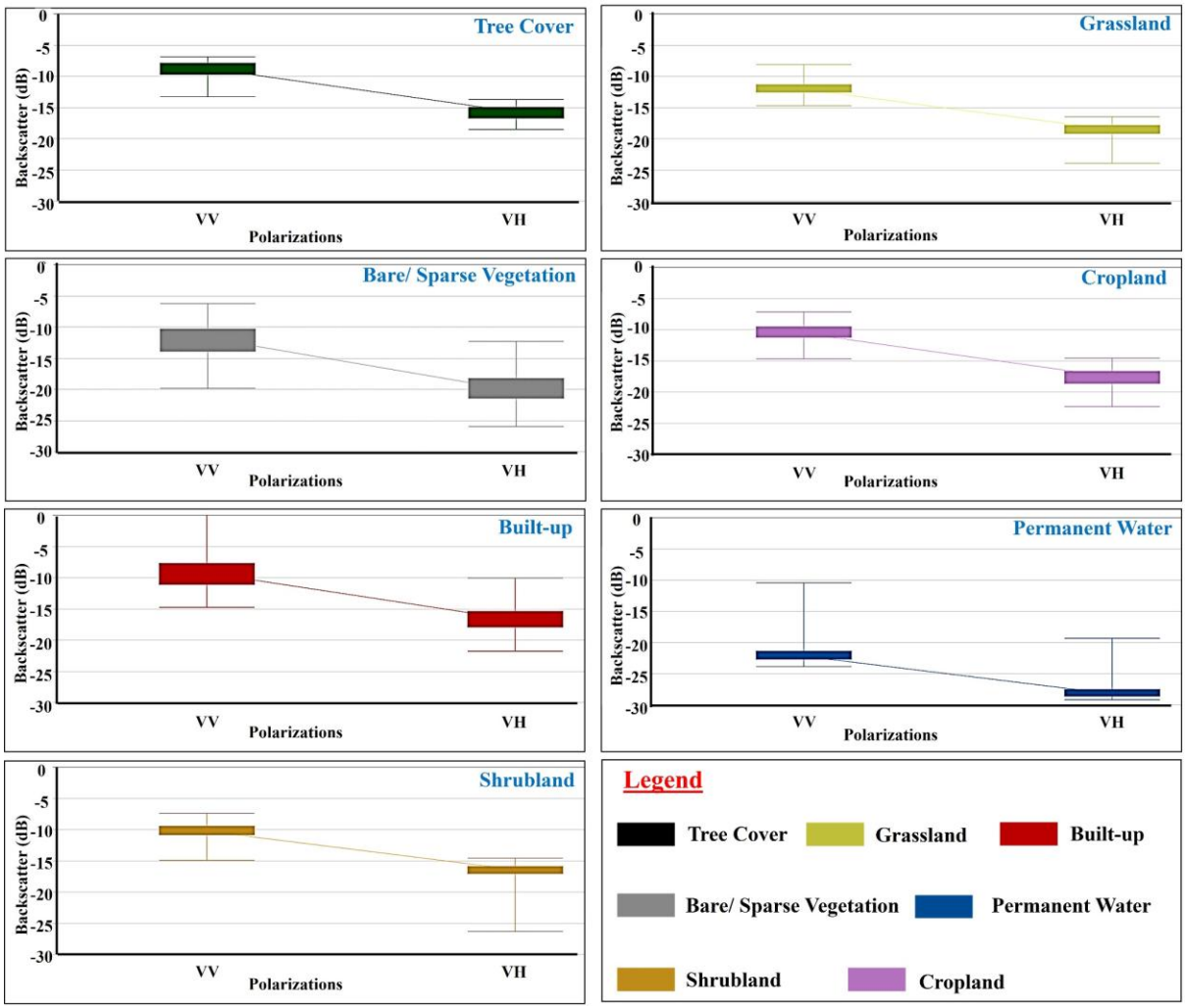


Figure 5. Boxplots of Sentinel-1 SAR backscatter coefficient (σ^0) distributions for different land cover/land use classes in the VV and VH polarizations.

3.1.5. Permanent water and steep-slope masking

To reduce the overestimation of flood extent, permanent water bodies were excluded from the preliminary flood map. For this purpose, the JRC Global Surface Water dataset, available through the GEE platform, was employed. Permanent water pixels were identified based on the long-term water occurrence frequency, where pixels with a water occurrence greater than the threshold τ were classified as permanent water according to Equation (11). The permanent-water threshold of 70% was selected because it effectively identifies persistent water bodies while avoiding the exclusion of seasonally inundated or temporary wetlands. This value has been commonly adopted in previous flood-mapping studies using the Global Surface Water dataset and provides a

suitable balance between omission and commission errors (Li, C. et al., 2022; Tripathy & Malladi, 2022). Nevertheless, the threshold can be adjusted according to regional hydrological characteristics and the objectives of individual applications. This step prevents permanent water bodies from being incorrectly identified as newly flooded areas, thereby reducing commission errors in the final flood map.

$$W_{perm}(p) = \begin{cases} 1 & Occ(p) \geq \tau \\ 0 & Occ(p) < \tau \end{cases} \tag{11}$$

In addition, a terrain slope mask was generated from the 30-m SRTM DEM Equation (12). Because floodwater accumulation is highly unlikely on steep terrain, areas with slopes greater than 15% were excluded from the final flood map.

$$Slope_{Mask}(p) = \begin{cases} 1 & slope(p) \geq \tau \\ 0 & slope(p) < \tau \end{cases} \tag{12}$$

This threshold has been widely adopted in previous flood mapping studies and has been shown to improve mapping accuracy by reducing false flood detections over mountainous regions (Farhadi et al., 2025a). Furthermore, from a hydrological perspective, steep slopes generally prevent water ponding, making such areas unsuitable for flood inundation. Finally, the preliminary flood map was refined by excluding permanent water bodies and steep-slope areas through the application of the permanent water and slope masks. The resulting map represents the final flood extent, as defined in Equation (13).

$$Flood_{Final}(p) = \left[Flood_{primary}(p) - W_{perm}(p) - Slope_{Mask}(P) \right] \tag{13}$$

Unlike conventional flood mapping approaches that rely on empirical thresholds or single-date SAR observations, the proposed framework establishes a historical backscatter baseline for each pixel using multi-temporal pre-flood Sentinel-1 observations. Flooding is subsequently identified as statistically significant deviations from this pixel-specific temporal behavior, forming the core innovation of the ATS-Flood framework. Although several parameters are employed within the proposed framework, they are physically interpretable rather than empirically optimized. Moreover, their values can be readily adapted to different climatic, hydrological, and topographic conditions without modifying the overall workflow.

4. Results and Discussion

This section presents the results of the proposed flood mapping framework. The performance of the proposed approach is then comprehensively evaluated through both qualitative and quantitative analyses using standard

accuracy assessment metrics. Finally, a comparative analysis is conducted against several existing flood mapping approaches to demonstrate the effectiveness, robustness, and generalization capability of the proposed framework.

4.1. Qualitative Assessment of the Proposed Framework

Figure 6 presents the flood extent delineated by the proposed framework over the study area. The post-flood Sentinel-1 SAR image was acquired on 8 March 2019, whereas the pre-flood reference image was generated by averaging all Sentinel-1 observations acquired during the one-month period preceding the flood event. The resulting flood map indicates that extensive inundation occurred across the western part of Khuzestan Province, primarily along the Karkheh, Karun, and Dez river systems. The spatial distribution of the detected flooded areas is consistent with the major river corridors, confirming that the flood propagation predominantly followed the downstream floodplains. Given the large spatial extent of the study area, five representative regions located along the main river channels were selected to provide a more detailed qualitative evaluation of the proposed framework (Figure 7).

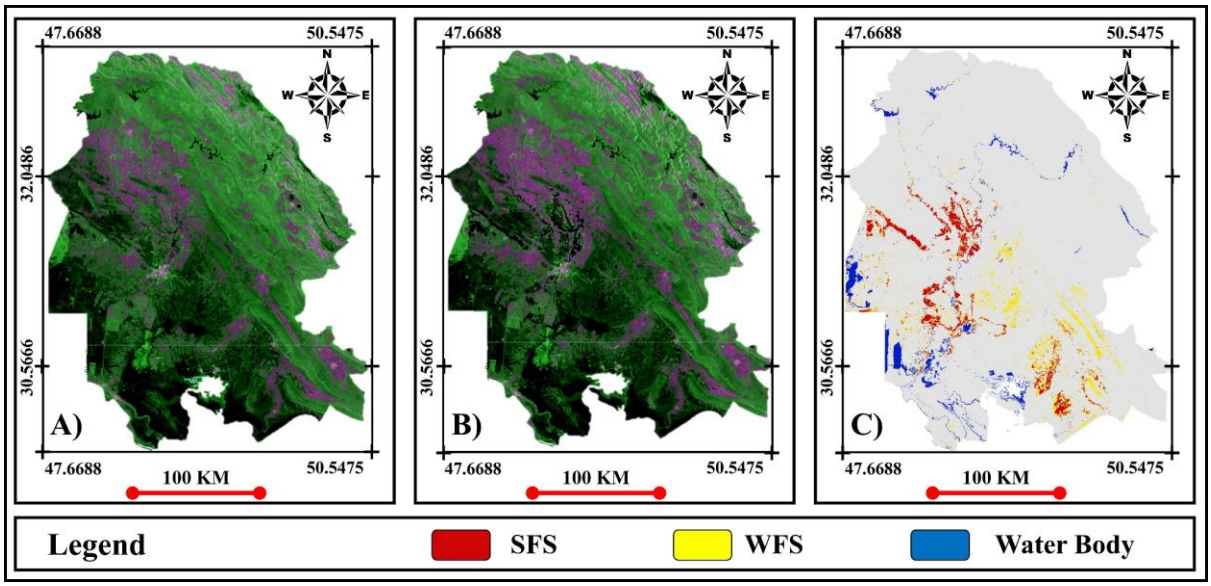


Figure 6. Flood mapping results produced by the proposed framework. (A) Mean pre-flood Sentinel-1 SAR image generated from observations acquired during the one-month period preceding the flood event, (B) post-flood Sentinel-1 SAR image acquired on 8 March 2019, and (C) resulting flood extent map.

These local-scale examples demonstrate that severe inundation occurred within agricultural lands adjacent to the rivers, while floodwater also extended into several developed and residential areas. Across all five representative regions, the proposed framework successfully delineated the flood boundaries and produced spatially coherent inundation patterns that closely matched the visual characteristics of the SAR imagery. Unlike conventional binary flood mapping approaches, the proposed framework distinguishes inundated pixels into two confidence levels, namely WFS and SFS. This dual-level representation provides additional information regarding

the strength of the flood-induced SAR response, enabling a more comprehensive interpretation of flood severity and spatial variability. Such information can support post-disaster damage assessment, emergency response, resource allocation, and risk-based decision-making, particularly in regions where flood intensity varies considerably across the affected area.

The qualitative results further reveal that agricultural lands experienced the most extensive inundation, reflecting the close proximity of cultivated areas to the major river channels. In addition, several urban settlements located near the rivers were also affected by floodwaters, indicating the vulnerability of developed areas situated within flood-prone floodplains. Figure 8 illustrates five representative cities where river overflow resulted in substantial inundation of surrounding urban environments.

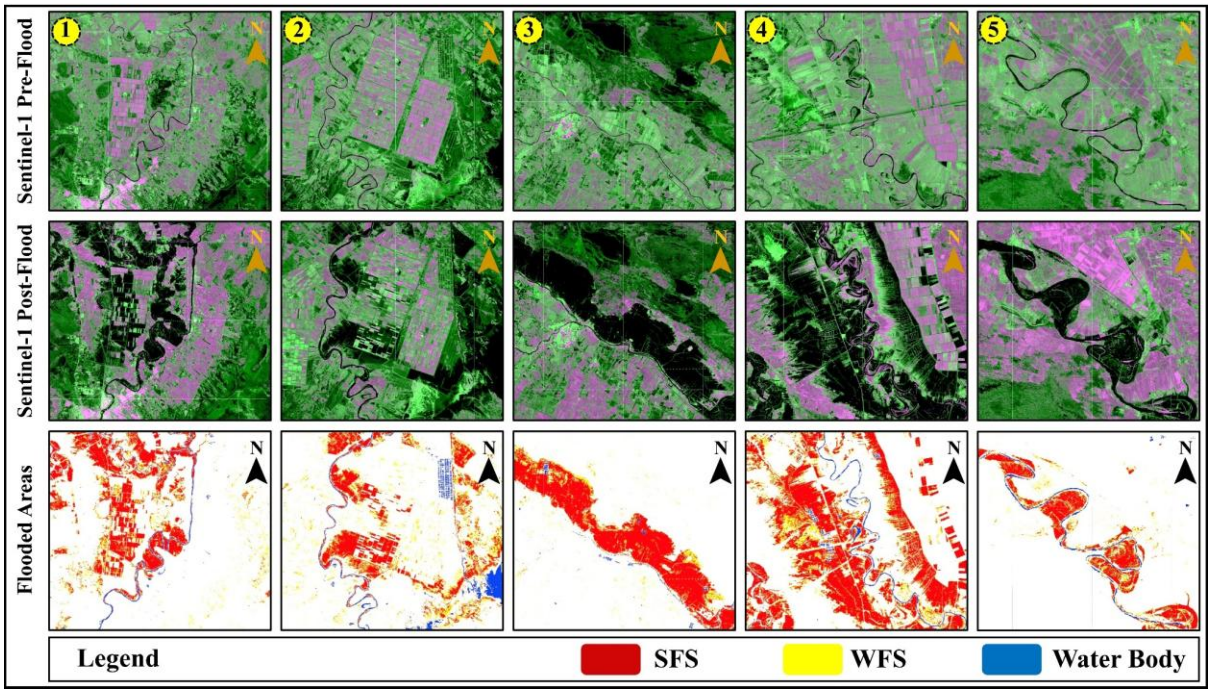


Figure 7. Qualitative flood mapping results produced by the proposed framework for five representative riverine regions. The first row shows pre-flood Sentinel-1 False-Color Composite (FCC) images, the second row presents the post-flood Sentinel-1 FCC images, and the third row illustrates the corresponding detected flood extent maps.

Overall, the proposed framework demonstrates a strong capability to visually discriminate flooded areas from surrounding land-cover classes while preserving the spatial continuity of inundated regions. Although the qualitative assessment confirms the effectiveness of the proposed methodology, a comprehensive quantitative evaluation using independent reference data and standard accuracy metrics is presented in the following sections. It is worth noting that SAR imagery acquired over urban environments is frequently affected by geometric distortions, such as radar shadow and layover, which may produce backscatter characteristics similar to open water and consequently increase false flood detections. By explicitly incorporating the historical backscatter

behavior of each pixel through the pre-flood time series, the proposed framework effectively suppresses these persistent radar artifacts and other stable urban scattering effects. Consequently, flood identification is driven primarily by statistically significant temporal anomalies rather than absolute backscatter values, resulting in improved robustness and a lower probability of misclassification in complex urban environments.

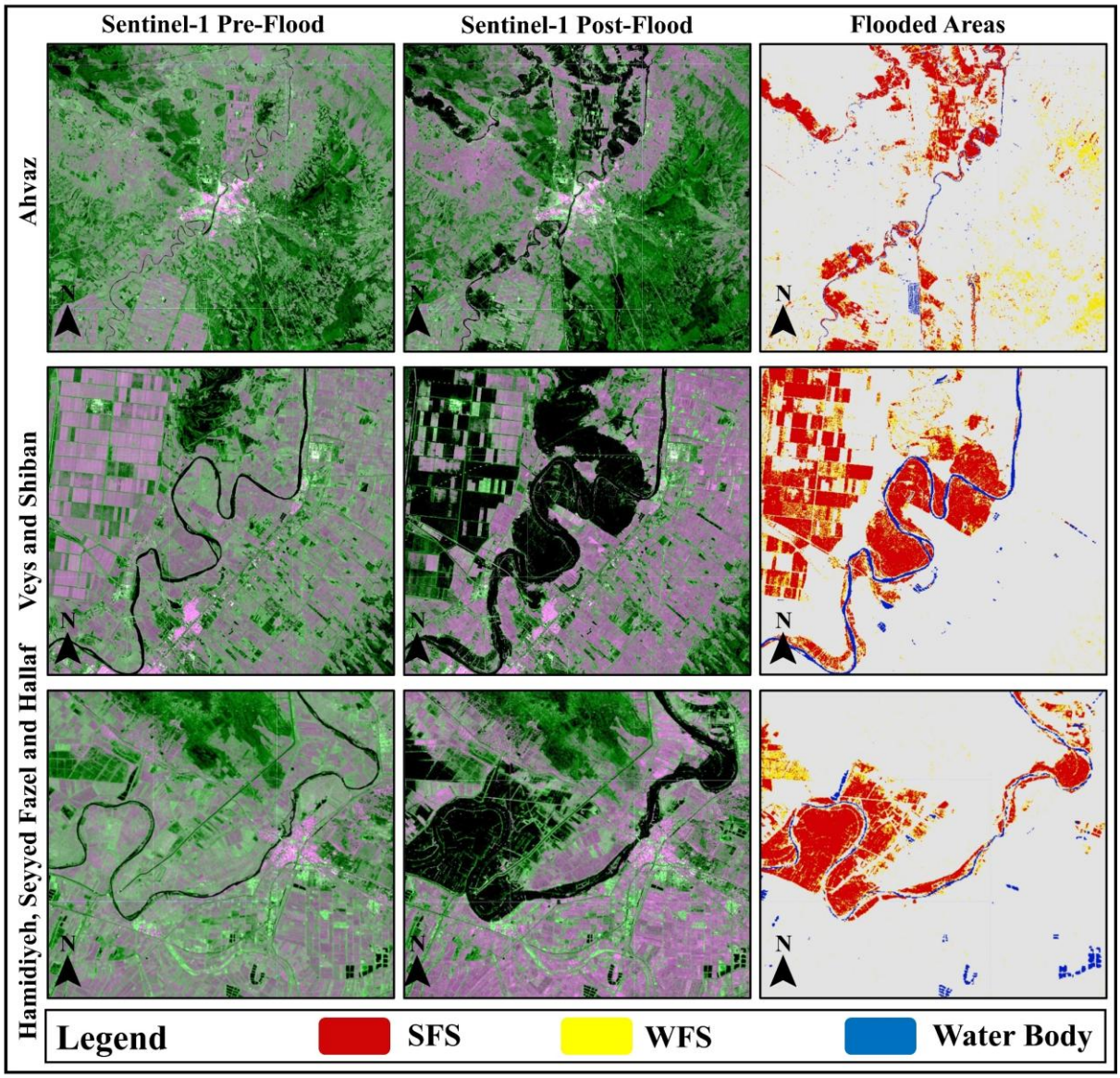


Figure 8. Flood extent detection results obtained using the proposed framework for five cities located along the river. The first column shows the pre-flood Sentinel-1 FCC, the second column presents the post-flood Sentinel-1 FCC images, and the third column displays the final extracted flood inundation maps.

4.2. Quantitative Assessment of the Proposed Framework

The qualitative assessment presented in the previous section demonstrated that the proposed framework provides visually reliable flood mapping results. However, qualitative interpretation alone is insufficient for a comprehensive performance evaluation; therefore, a quantitative accuracy assessment was also conducted. In this study, reference data from the Copernicus EMS, high-resolution Google Earth imagery, and Sentinel-2 images

were used for validation. The spatial distribution of the validation samples is illustrated in Figure 9, showing that the samples are well distributed across the study area and represent diverse geographic conditions.

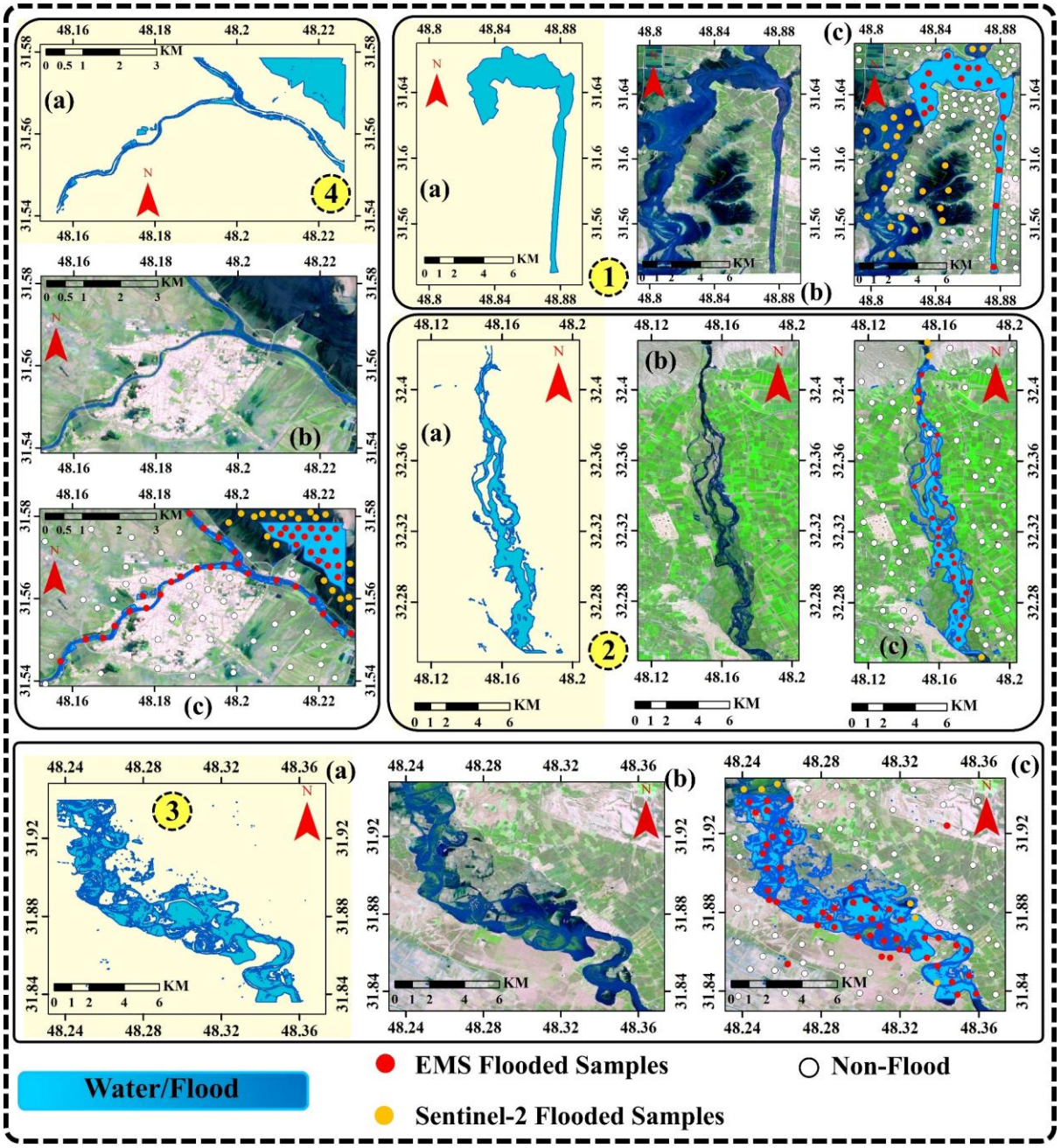


Figure 9. Spatial distribution of the validation samples used for accuracy assessment of the proposed ATS-Flood across four representative regions within the study area: (a) Copernicus EMS reference flood maps, (b) Sentinel-2 optical imagery, and (c) overlay of the EMS reference data and Sentinel-2 imagery.

To quantitatively evaluate the performance of the proposed framework, five widely used accuracy metrics were calculated, including Overall Accuracy (OA) (Equation 14), Producer's Accuracy (PA) (Equation 15), User's Accuracy (UA) (Equation 16), F1-score (Equation 17), and the Kappa coefficient (Equation 18).

$$\mathrm{OA} = \frac{TP + TN}{TP + TN + FP + FN} \tag{14}$$

$$\mathrm{PA} = \frac{TP}{TP + FN} \tag{15}$$

$$\mathrm{UA} = \frac{TP}{TP + FP} \tag{16}$$

$$F1 - Score = \frac{2TP}{2TP + FP + FN} \tag{17}$$

$$P_e = \frac{(TP + FP)(TP + FN) + (FN + TN)(FP + TN)}{(TP + TN + FP + FN)^2}, \quad P_o = \frac{TP + TN}{TP + TN + FP + FN} \Rightarrow \kappa = \frac{P_o - P_e}{1 - P_e} \tag{18}$$

A quantitative assessment was conducted using a total of 4,000 validation samples, including 2,000 flood and 2,000 non-flood points. The results demonstrate the high reliability and robustness of the proposed framework in discriminating flooded from non-flooded areas. As summarized in Table 1, the proposed framework achieved an OA of 93.25%, indicating excellent classification performance over the study area. The PA and UA for the flood class reached 92.5% and 93.9%, respectively, demonstrating that the majority of flooded pixels were correctly identified while maintaining a low false-positive rate. Similarly, the corresponding accuracy metrics for the non-flood class confirm a well-balanced classification performance between the two classes. Furthermore, the proposed framework achieved a KC of 0.865, indicating an excellent level of agreement beyond chance, while the F1-score of 93.2% confirms a favorable balance between precision and recall. These results demonstrate that incorporating historical Sentinel-1 SAR observations to characterize the normal backscatter behavior of each pixel substantially improves flood detection accuracy by reducing false alarms associated with permanent radar artifacts and heterogeneous land-cover conditions. Overall, the proposed ATS-Flood framework provides reliable flood extent mapping with an accuracy exceeding 93%, highlighting its potential for rapid and operational flood monitoring over large-scale regions.

Table 1. Quantitative accuracy assessment results of the proposed flood detection algorithm

Class	Number of Validation Samples	F1-Score (%)	PA (%)	UA (%)	KC	OA (%)
Flood	2000	93.2	92.5	93.9	0.865	93.25
Non-Flood	2000	93.3	94	92.6		

4.3. Sensitivity analysis of threshold selection

To evaluate the robustness of the proposed framework with respect to threshold selection, a sensitivity analysis was conducted by comparing manual thresholding with the automatic Otsu method. The corresponding results are presented in Figure 10. Figures 10(a) and 10(b) illustrate the histograms of the SCV (Z-values) for the VV and VH polarizations, respectively. In both cases, most pixels are concentrated around zero, representing stable non-flooded areas, whereas flooded pixels form the left tail of the distributions due to the significant decrease in SAR backscatter after inundation. For the VV polarization, the manually selected threshold was approximately −2.70, while the Otsu algorithm automatically determined a threshold of about −2.45. Similarly, for the VH polarization, the manual and Otsu thresholds were approximately −2.70 and −2, respectively. These results indicate that the Otsu method tends to select slightly fewer conservative thresholds, resulting in a larger number of pixels being classified as flooded. As visually illustrated in Figure 10(f) and (g), this leads to a slightly larger mapped flood extent (specifically in WFS) compared with the manually selected thresholds. Nevertheless, the differences are limited, confirming that the automatic Otsu thresholding approach provides reliable flood delineation while eliminating the need for subjective threshold selection.

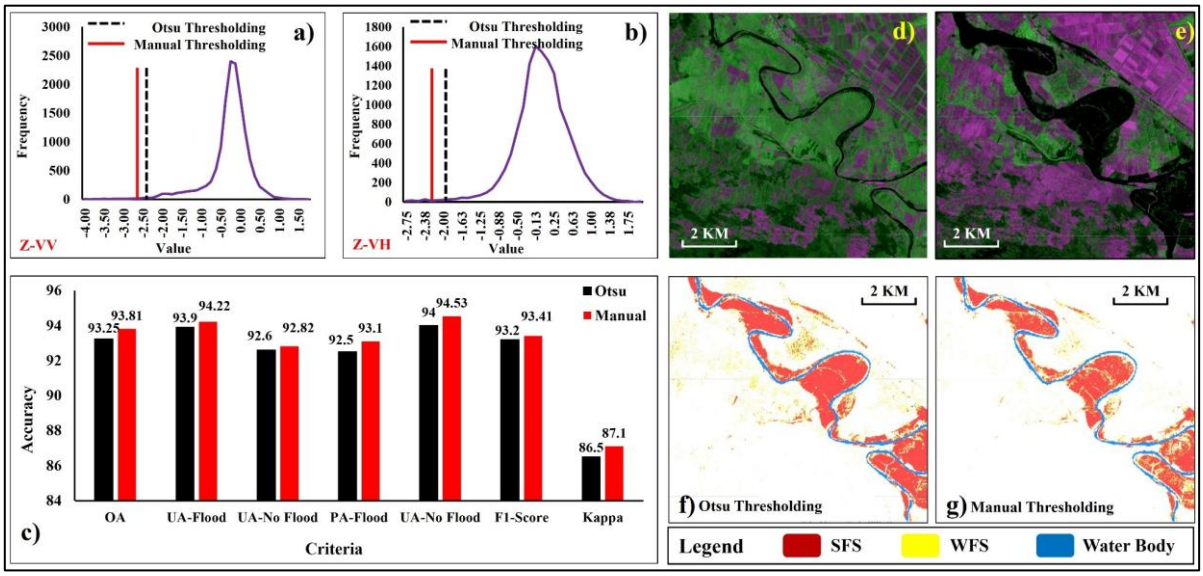


Figure 10. Sensitivity analysis of threshold selection for flood mapping based on the proposed framework. Histograms of Z-values for (a) VV and (b) VH polarizations, showing the manually selected threshold and the automatically determined Otsu threshold; (c) comparison of quantitative accuracy metrics obtained using the two thresholding approaches; (d) pre-flood Sentinel-1 image; (e) post-flood Sentinel-1 image; (f) flood extent derived using the Otsu threshold; and (g) flood extent derived using the manually selected (trial-and-error) threshold.

To assess the impact of threshold selection on flood mapping accuracy, the quantitative performance of both approaches was compared (Figure 10(c)). The manually selected thresholds achieved a slightly higher Overall Accuracy (93.81%) than the automatic Otsu approach (93.25%). A similar trend was observed for the Kappa coefficient, which increased from 0.865 to 0.871 when manual thresholds were used. The User's Accuracy for the

flood class improved marginally from 93.9% to 94.22%, while the F1-score increased from 93.2% to 93.41%. Despite these small improvements, the differences between the two approaches remained below 1% for all evaluation metrics. Overall, the sensitivity analysis demonstrates that although manual threshold selection provides a marginal improvement in classification accuracy, the automatic Otsu method achieves nearly equivalent performance while eliminating subjective parameter tuning. Therefore, considering its full automation, computational efficiency, and reproducibility, the Otsu-based thresholding strategy was adopted in the proposed framework. It should be noted that the thresholding procedure represents only the final decision step, whereas the discrimination capability of ATS-Flood primarily originates from the temporal characterization of each pixel. By modeling historical backscatter variations prior to thresholding, the proposed framework substantially reduces the influence of scene-dependent fluctuations before flood classification is performed.

4.4. Sensitivity analysis of the slope threshold

The influence of the slope mask threshold on flood detection accuracy was also investigated, and the results are presented in Figure 11. Four evaluation metrics, including OA, (PA, UA, and the KC, were calculated for different slope thresholds. As shown in Figure 11, increasing the slope threshold from low values to approximately 6% substantially improved all accuracy metrics, with the OA increasing from near zero to above 90%. Beyond this value, the evaluation metrics became relatively stable, exhibiting only minor fluctuations. Although the highest accuracy was observed around the 8% threshold (Region B), its improvement over the 15% threshold (Region A) was negligible and within the expected statistical variation. Considering both classification accuracy and model robustness, a 15% slope threshold was selected for the proposed framework.

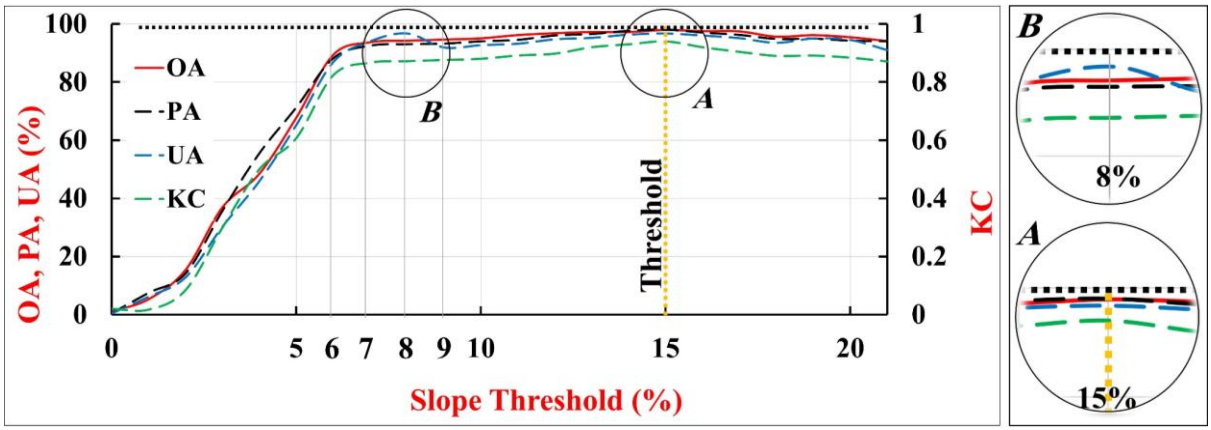


Figure 11. Sensitivity analysis of the slope-threshold mask on flood detection accuracy. The plots illustrate the variation of the evaluation metrics with different slope thresholds. Insets (A) and (B) show enlarged views of the corresponding sections of the curves to highlight the differences between threshold values.

This threshold effectively removes steep terrain where flood accumulation is physically unlikely while maintaining high mapping accuracy and improving the general applicability of the method across different landscapes.

4.5. Performance Across Orbit Configurations

Figure 12 presents the flood detection results obtained from the proposed framework using Sentinel-1 SAR images acquired from ascending, descending, and combined ascending–descending orbits. As highlighted by the boxed regions in the figure, the flood maps generated from a single acquisition geometry (ascending or descending) do not provide consistently reliable results from a visual perspective. In some locations, the ascending orbit successfully delineates flooded areas, whereas the descending orbit exhibits omission or commission errors. Conversely, in other locations the descending orbit performs better while the ascending acquisition introduces misclassification. These inconsistencies mainly arise from the side-looking geometry of SAR sensors, where the backscatter response is strongly influenced by the imaging geometry, surface roughness, local incidence angle, and vegetation structure. Consequently, the sensitivity of a single orbit to soil moisture and localized scattering mechanisms may lead to false flood detections or missed flooded areas.

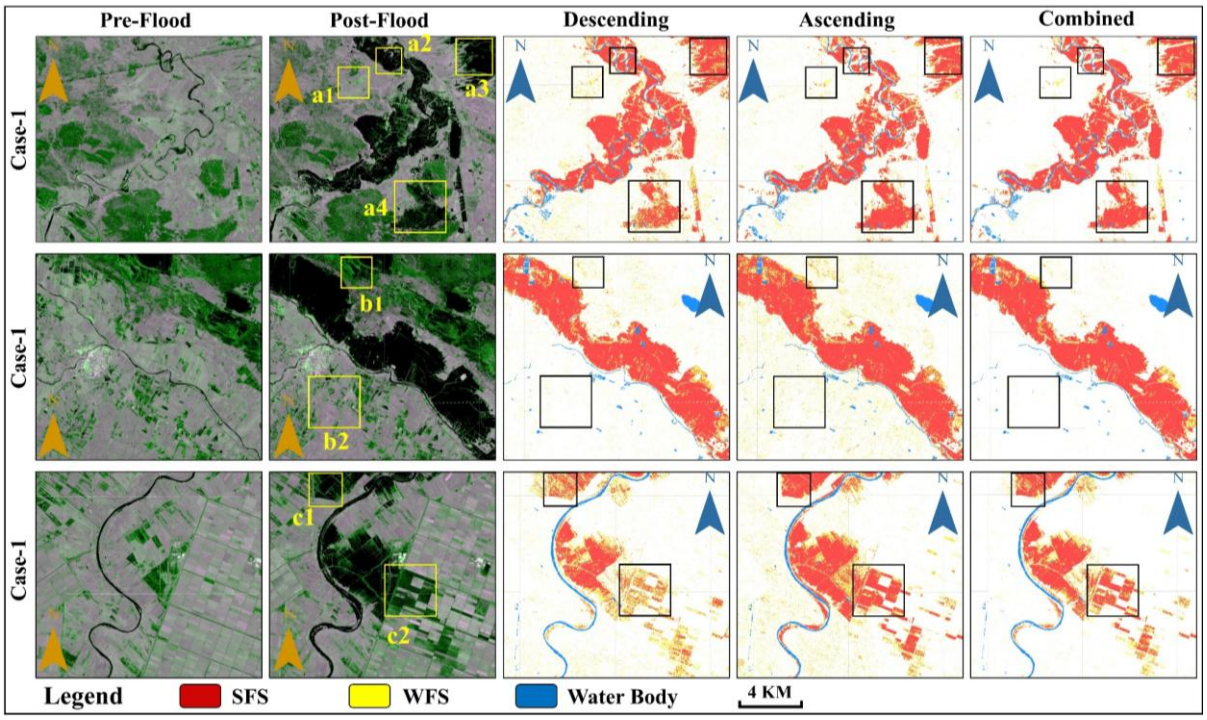


Figure 12. Visual comparison of flood detection using ascending, descending, and combined Sentinel-1 observations. The highlighted boxes indicate representative areas where flood mapping differs among the three orbit configurations.

In contrast, the combined ascending–descending dataset substantially reduces these orbit-dependent effects by integrating complementary observations acquired from opposite viewing geometries. As a result, random noise,

local moisture-induced artifacts, and geometric distortions are mitigated, leading to a more spatially consistent and reliable flood extent map. Visual inspection indicates that the combined approach produces cleaner flood boundaries and significantly fewer false detections than either single-orbit dataset.

Figure 13 presents the quantitative performance comparison of the proposed framework using ascending, descending, and combined Sentinel-1 observations. As shown in Figure 12(a), the combined observations consistently achieved the highest accuracy across all evaluation metrics. The OA increased from 91.4% and 90.9% for the ascending and descending acquisitions to 93.25% for the combined dataset. Similarly, the PA and UA improved to 92.5% and 93.9%, respectively, while the F1-score reached 93.2%. The most noticeable improvement was observed for the KC, which increased from 82.8% and 82.1% to 86.5%, indicating a considerably higher agreement with the reference data. The relative improvements achieved by the combined observations are summarized in Figure 12(b). Compared with the ascending acquisition, the combined approach improved OA, PA, UA, and F1-score by approximately 1.8–2.0%, whereas the improvement over the descending acquisition ranged between 2.3% and 2.6%. The largest gain was obtained for the KC, reaching 3.7% and 4.4% compared with the ascending and descending datasets, respectively. These results demonstrate that integrating observations from both orbit directions not only improves classification accuracy but also enhances the statistical consistency of the flood map.

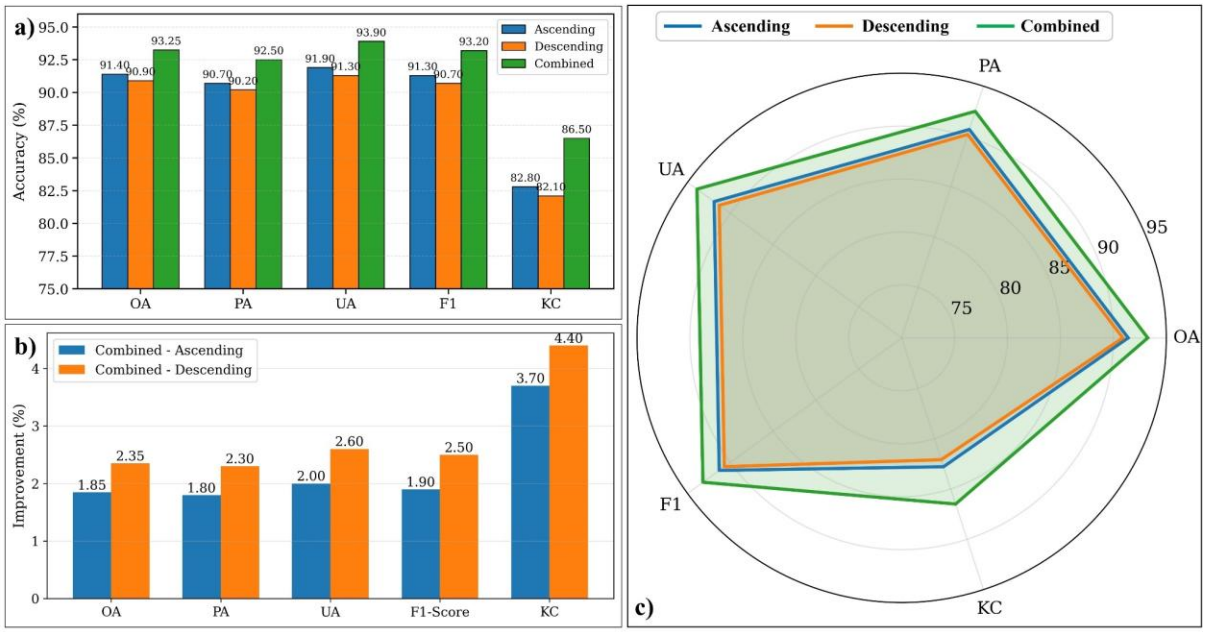


Figure 13. Quantitative evaluation of the proposed flood detection framework using ascending, descending, and combined Sentinel-1 observations. a) Comparison of the segmentation accuracy metrics obtained from the three acquisition strategies. b) Percentage improvement achieved by the combined observations relative to the

ascending and descending acquisitions. c) Radar chart summarizing the overall performance, demonstrating the consistent superiority and balanced accuracy of the combined observations across all evaluation metrics.

The radar chart in Figure 12(c) further confirms the superior and more balanced performance of the combined observations across all evaluation metrics. Unlike the ascending and descending acquisitions, whose performance varies depending on the imaging geometry and local surface conditions, the combined dataset consistently outperforms both individual configurations. This behavior can be attributed to the complementary viewing geometries of ascending and descending Sentinel-1 acquisitions, which reduce orbit-dependent effects such as moisture sensitivity, geometric distortions, layover, shadowing, and local backscatter variability. Consequently, averaging observations from both orbit directions suppresses random fluctuations and scene-dependent noise, resulting in a more robust representation of the surface backscatter and, therefore, more reliable flood delineation. Overall, these quantitative results corroborate the qualitative observations presented in the previous section and demonstrate that integrating ascending and descending Sentinel-1 observations significantly enhances the robustness, stability, and generalization capability of the proposed flood detection framework. It is noteworthy that neither the ascending nor the descending acquisition consistently outperformed the other across different flood scenes. Instead, their relative performance depended on the local imaging geometry and land surface characteristics. This observation highlights the limitation of relying on a single orbit direction and further justifies the use of the combined observations in the proposed framework.

4.6. Comparative Analysis of the Proposed Framework with other Methods

The qualitative comparison between the proposed framework and the benchmark flood detection methods, including S1-VV, S1-VH, SDWI (Du et al., 2023), NDFI-VV, NDFI-VH (Cian et al., 2018), UN-VV, UN-VH (Canty & Nielsen, 2017; UN-SPIDER, 2021), and SBFD (Farhadi et al., 2025b), is presented in Figure 14. Two representative flood scenes were selected to visually evaluate the capability of each method in delineating inundated areas under different surface conditions. As illustrated in Case 1, the proposed framework successfully delineates the flooded regions while effectively suppressing false detections over non-flooded areas. In contrast, the UN-VV, NDFI-VH, and NDFI-VV methods exhibit noticeable overestimation, incorrectly classifying several non-flooded pixels as flooded. The remaining methods produce relatively reasonable flood maps; however, they still contain isolated misclassifications and exhibit lower spatial consistency compared with the proposed approach. A similar pattern is observed in Case 2. The UN-VV, UN-VH, and SBFD methods underestimate the inundated extent, resulting in the omission of several flooded regions located along the river boundaries. Conversely, NDFI-VH again shows excessive overestimation, leading to numerous false flood detections over

surrounding land-cover classes. These observations indicate that the performance of existing methods is highly dependent on local backscatter characteristics and environmental conditions, making them susceptible to both commission and omission errors.

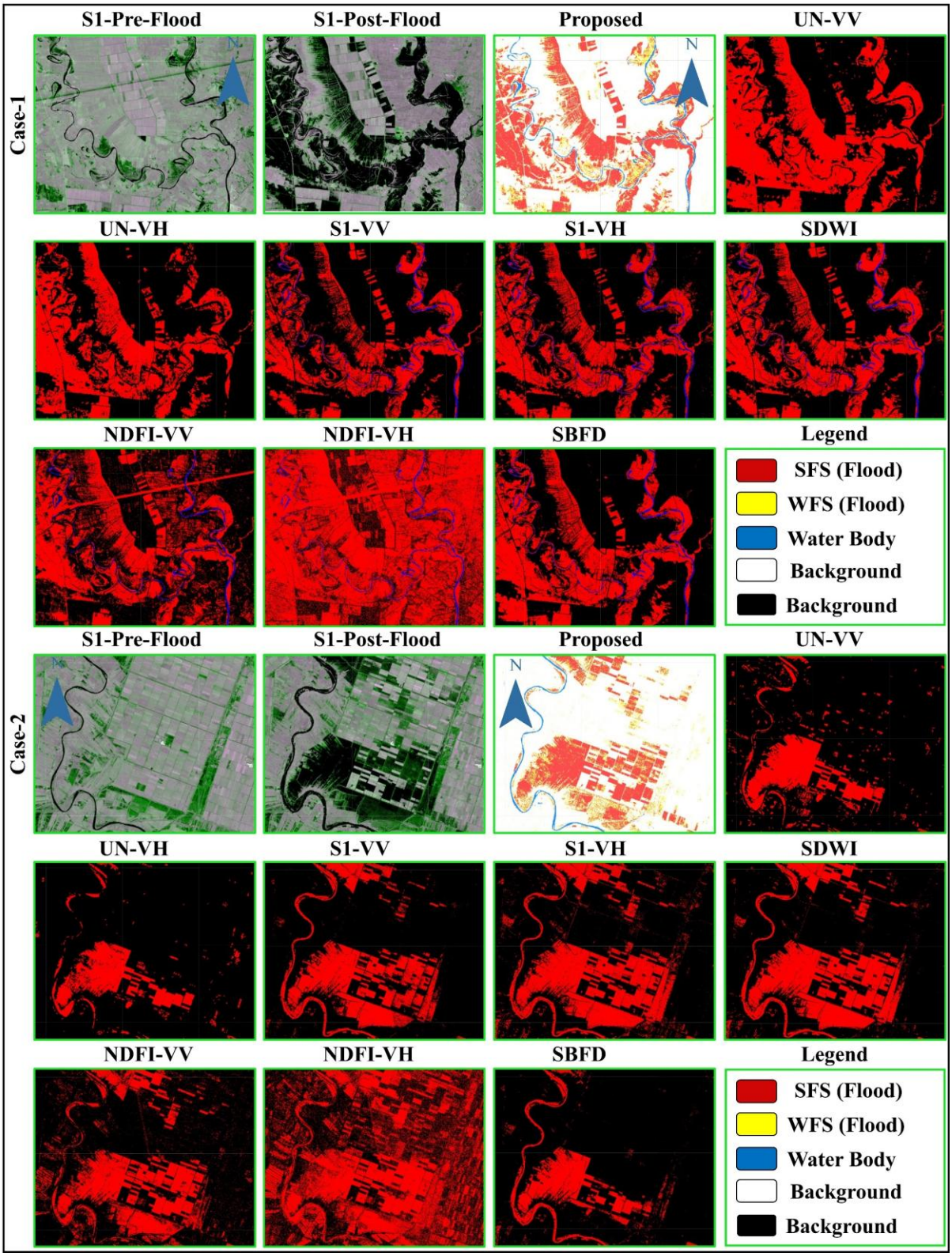
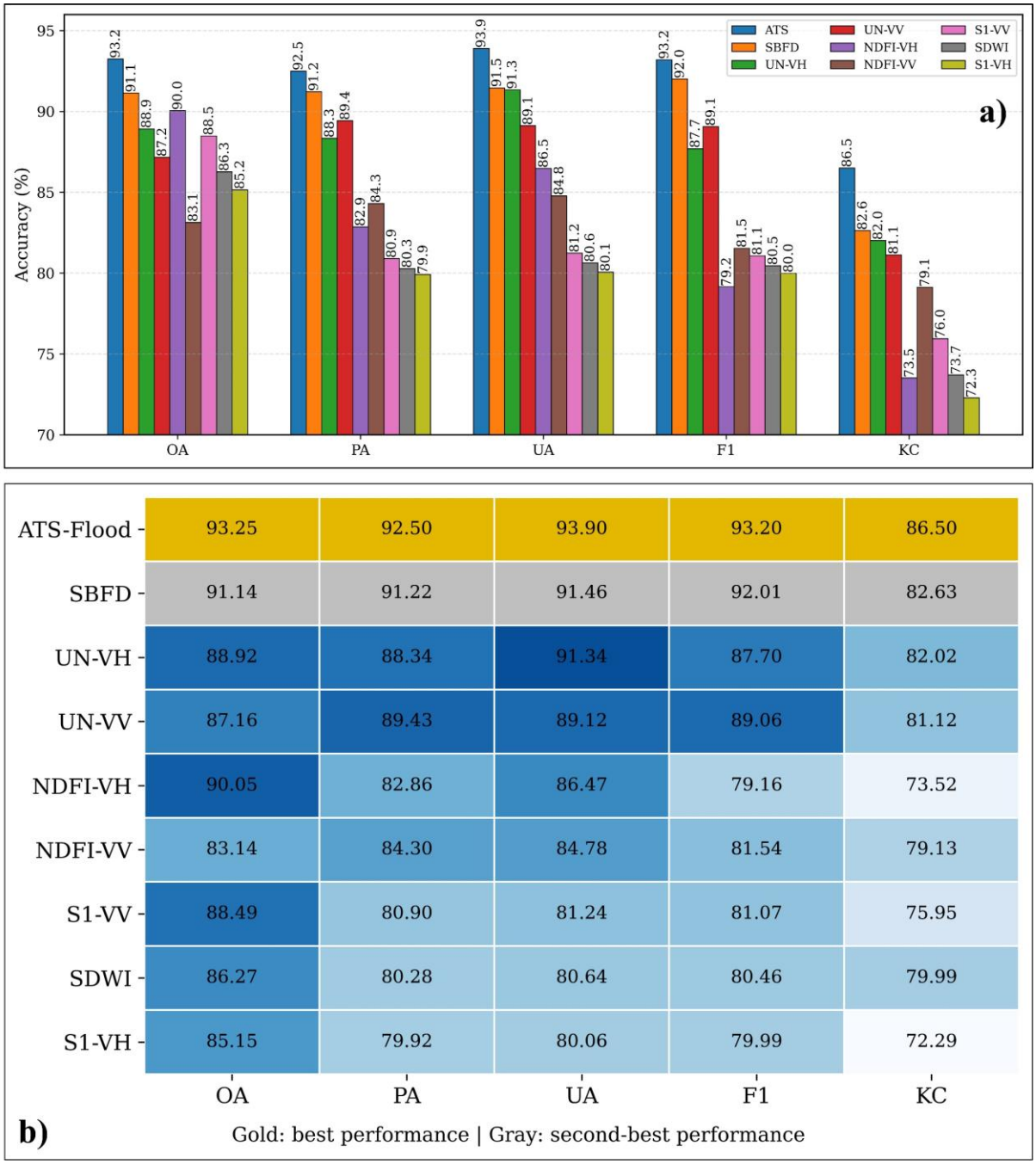


Figure 14. Qualitative comparison of flood extent maps produced by the proposed ATS-Flood framework and benchmark methods for two representative areas.

The observed differences can be explained by the underlying principles of the compared methods. Single-polarization approaches (S1-VV and S1-VH) rely exclusively on the backscatter intensity of one SAR polarization and therefore cannot adequately distinguish flood-induced changes from other sources of backscatter variability, such as soil moisture fluctuations, vegetation structure, or surface roughness. Similarly, NDFI- and SDWI-based indices are primarily driven by empirical backscatter relationships and remain sensitive to scene heterogeneity, often leading to overestimation or underestimation in heterogeneous landscapes.



	OA	PA	UA	F1	KC
ATS-Flood	93.25	92.50	93.90	93.20	86.50
SBFD	91.14	91.22	91.46	92.01	82.63
UN-VH	88.92	88.34	91.34	87.70	82.02
UN-VV	87.16	89.43	89.12	89.06	81.12
NDFI-VH	90.05	82.86	86.47	79.16	73.52
NDFI-VV	83.14	84.30	84.78	81.54	79.13
S1-VV	88.49	80.90	81.24	81.07	75.95
SDWI	86.27	80.28	80.64	80.46	79.99
S1-VH	85.15	79.92	80.06	79.99	72.29

Figure 15. Quantitative comparison of the proposed ATS-Flood framework with benchmark flood mapping methods. (a) Comparison of OA, PA, UA, F1-score, and KC. (b) Relative performance improvement of ATS-Flood over each benchmark method in terms of OA, F1-score, PA, UA and KC.

Although the UN-based approaches incorporate change detection, they are fundamentally dependent on the selection of a single pre-flood reference image. Consequently, natural temporal variations unrelated to flooding may be incorrectly interpreted as flood signals. In contrast, ATS-Flood models the historical backscatter behavior of each pixel using multi-temporal Sentinel-1 observations, allowing flood detection to be based on statistically significant deviations from long-term conditions rather than on absolute backscatter values or single-date differences. The quantitative comparison is summarized in Figure 15. Consistent with the visual assessment, the proposed ATS-Flood framework achieves the highest performance across all evaluation metrics. Specifically, it attains an OA of 93.25%, a PA of 92.50%, a UA of 93.90%, an F1-score of 93.20%, and a KC of 86.50%, outperforming all competing approaches.

Figure 16 further quantifies the performance gain of the proposed ATS-Flood framework over the benchmark methods in terms of OA, F1-score, and KC. As illustrated, SBFD is the closest competitor, with performance differences limited to 2.1%, 1.2%, and 3.9 percentage points for OA, F1-score, and KC, respectively. Despite this relatively small margin, ATS-Flood consistently outperforms SBFD across all evaluation metrics. More substantial improvements are observed for the remaining approaches. Compared with the UN-based methods, the proposed framework increases OA by 4.3–6.1%, while the F1-score and KC improvements range from 4.1–5.5% and 4.5–5.4 percentage points, respectively. Even larger performance gains are achieved over the NDFI- and single-polarization-based methods. In particular, ATS-Flood improves the F1-score by up to 14% over NDFI-VH and by 13.2% over S1-VH, while the corresponding KC improvements reach 13 and 14.2 percentage points, respectively. Similar trends are observed for OA, where the proposed framework exceeds conventional methods by 7–10 percentage points, highlighting the substantial improvement achieved by the proposed strategy. These results demonstrate that the performance advantage of ATS-Flood is not limited to a single evaluation metric but is consistently maintained across accuracy, class balance, and agreement statistics. The superior performance of ATS-Flood is primarily attributed to its pixel-wise temporal modeling strategy. By establishing a historical backscatter baseline from multiple pre-flood Sentinel-1 observations, the proposed framework effectively separates flood-induced backscatter reductions from normal temporal fluctuations caused by rainfall, soil moisture variability, vegetation phenology, and agricultural activities. Consequently, natural seasonal changes are less likely to be misclassified as flooding. Furthermore, the integration of VV and VH polarizations exploits complementary scattering mechanisms, improving flood discrimination over different land-cover types. The Otsu thresholding further eliminates the subjectivity associated with manual threshold selection, while the permanent-water and terrain-slope masks reduce false alarms over rivers, reservoirs, and steep terrain. The combined effect

of these components results in consistent improvements across all evaluation metrics rather than improvements limited to a single accuracy measure.

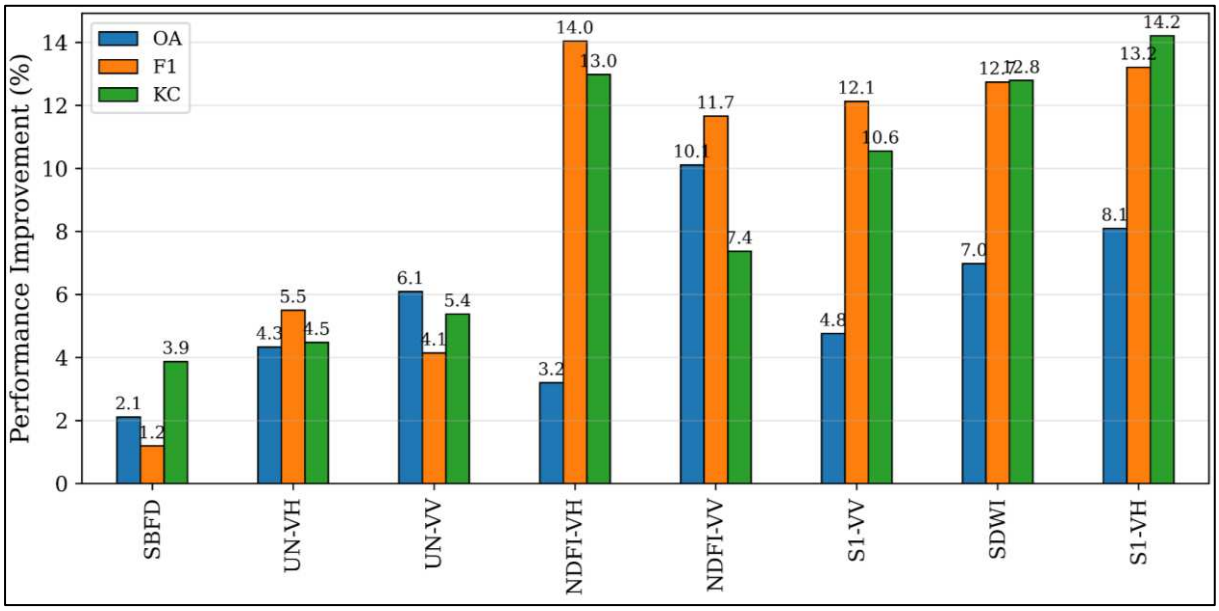


Figure 16. Relative performance improvement of the proposed ATS-Flood framework over the benchmark methods. The improvement values are expressed as the percentage gain achieved by ATS-Flood with respect to each competing method.

To further investigate the relationship among the evaluation metrics of the proposed framework and the benchmark methods are jointly visualized in Figure 17. In this figure, the horizontal axis represents OA, the vertical axis corresponds to KC, while the color intensity indicates UA (Figure 17a) and PA (Figure 17b), respectively. As illustrated, the proposed ATS-Flood framework is clearly separated from the remaining approaches and occupies the upper-right corner of both scatter plots, indicating the highest OA together with the strongest agreement beyond chance. In addition, the color scale confirms that ATS-Flood simultaneously achieves the highest user's and producer's accuracies, demonstrating that the proposed framework effectively minimizes both commission and omission errors. Among the benchmark methods, SBFD exhibits the closest performance to ATS-Flood, whereas the UN- and NDFI-based approaches form an intermediate group with moderate OA and KC values. In contrast, the conventional single-polarization methods (S1-VV and S1-VH) and the SDWI index are concentrated in the lower-left region of the plots, reflecting comparatively weaker classification performance and lower agreement with the reference data.

The distribution of the methods in the OA–KC feature space further reveals that improvements in ATS-Flood are systematic rather than incidental. Unlike the competing approaches, which generally exhibit a trade-off between OA and class-specific accuracy, ATS-Flood consistently maintains high OA, KC, UA, and PA

simultaneously. This balanced performance indicates a superior capability to preserve flood boundaries while suppressing false alarms, demonstrating the robustness and generalization ability of the proposed framework across different flood scenarios. Unlike conventional threshold-based methods, whose decision boundaries remain fixed across different acquisition conditions, ATS-Flood dynamically adapts to the historical behavior of each individual pixel. This capability substantially improves the transferability of the framework across different flood events, land-cover types, and imaging conditions. Consequently, the proposed method is less dependent on local calibration and is expected to provide more stable performance in large-scale operational flood mapping applications.

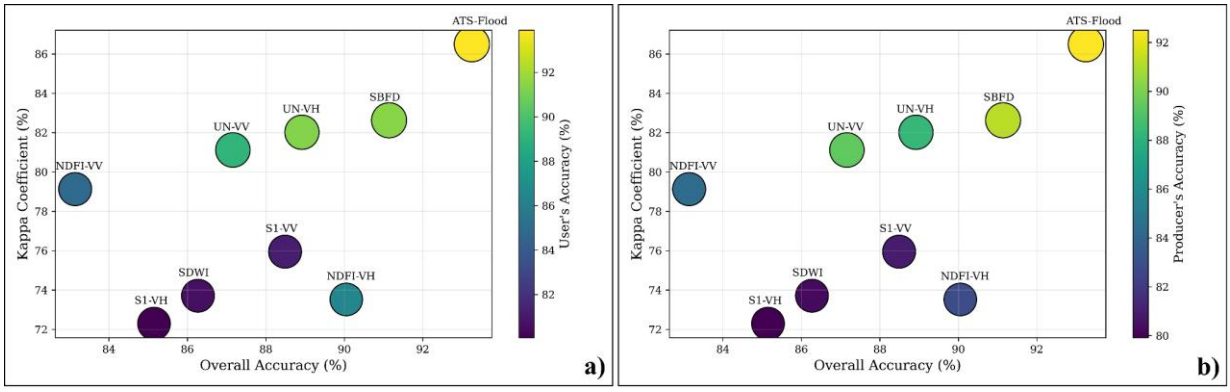


Figure 17. Relationship between OA and KC for the proposed ATS-Flood framework and benchmark methods. Marker color represents (a) UA and (b) PA, illustrating the overall classification performance and the balance between commission and omission errors.

4.7. Advantages and Disadvantages of the Proposed Framework

The proposed ATS-Flood framework offers several advantages over conventional SAR-based flood mapping approaches. First, unlike single-date or index-based methods that rely on fixed backscatter thresholds, the proposed framework models the normal backscatter behavior of each pixel using multi-temporal pre-flood Sentinel-1 observations. This temporal characterization significantly reduces the influence of scene-dependent backscatter variations and enables flood detection based on actual deviations from the historical signal rather than absolute intensity values. A second advantage is the complementary use of both VV and VH polarizations. The experimental results demonstrated that flood maps generated from either ascending or descending Sentinel-1 acquisitions individually may produce inconsistent results due to differences in acquisition geometry, vegetation structure, soil moisture conditions, and local scattering mechanisms. By integrating both observations (in ascending and descending), the proposed framework effectively suppresses polarization-specific noise and scene-dependent artifacts, resulting in more robust and spatially consistent flood delineation. Another important strength

of the proposed framework is its fully automatic processing chain. The incorporation of Otsu adaptive thresholding eliminates the need for manual threshold selection, thereby improving repeatability and facilitating large-scale and long-term flood monitoring. Furthermore, the application of permanent-water and terrain-slope masks substantially reduces commission errors over rivers, lakes, and mountainous regions without introducing additional user-defined parameters. The proposed framework also provides additional information by distinguishing flooded areas into SFS and WFS classes. Unlike conventional binary flood maps, this classification offers a more informative representation of flood severity and backscatter response, which may support post-disaster damage assessment, emergency response prioritization, and insurance-related applications. The quantitative evaluation further confirms these advantages. The proposed framework achieved the highest OA, F1-score, UA, and PA among all evaluated methods while maintaining a balanced performance across different flood scenarios. The comparison with existing approaches indicates that ATS-Flood consistently reduces both omission and commission errors, demonstrating its robustness under diverse land-cover conditions.

Despite its strong performance, several limitations should be acknowledged. The proposed framework requires a sufficient archive of pre-flood Sentinel-1 images to establish reliable temporal statistics. Consequently, its performance may decrease in regions where historical SAR observations are sparse, irregular, or unavailable, limiting the ability to accurately characterize the normal backscatter behavior of individual pixels. In addition, although the integration of ascending and descending observations considerably improves robustness, the current implementation assumes that both acquisition geometries are available within a short temporal interval. This assumption may not be satisfied during rapidly evolving flood events, where water levels change substantially between consecutive satellite acquisitions. Furthermore, the proposed framework may experience reduced accuracy in environments characterized by dense vegetation, extensive forest cover, or highly dynamic agricultural landscapes, where seasonal vegetation growth, harvesting activities, or crop rotation can produce backscatter variations similar to flood-induced changes. Finally, the framework relies exclusively on SAR observations. Although SAR imagery provides reliable all-weather monitoring capabilities, integrating complementary optical imagery, topographic information, or machine/deep learning techniques could further improve flood characterization, particularly in complex urban areas and heterogeneous floodplain environments.

Nevertheless, these limitations do not diminish the validity or practical applicability of the proposed framework. The consistent results obtained from the qualitative assessment, quantitative validation, sensitivity analyses, and comparisons with state-of-the-art flood mapping methods demonstrate that ATS-Flood provides accurate, robust, and reliable flood delineation under diverse environmental conditions. Therefore, the identified

limitations should be regarded primarily as opportunities for future improvements rather than constraints on the effectiveness of the proposed methodology.

Overall, ATS-Flood provides an effective balance between automation, accuracy, and computational efficiency for operational SAR-based flood mapping. Because the proposed framework models the historical temporal behavior of individual pixels rather than relying on region-specific thresholds or locally trained models, its methodology is inherently transferable and is expected to perform reliably across different flood-prone regions and climatic conditions. Nevertheless, additional validation is recommended before operational implementation in environments characterized by dense forest canopies, rapidly changing agricultural practices, or highly dynamic land-cover conditions, where temporal SAR backscatter may be influenced by processes other than flooding. Future research will focus on integrating additional SAR missions, optical satellite observations, and machine/deep learning techniques to further improve the applicability and robustness of the framework across diverse hydrological and environmental settings.

5. Conclusion

Flood mapping using SAR imagery remains challenging due to speckle effect, temporal backscatter variability, soil moisture fluctuations, and the complex scattering behavior of heterogeneous land-cover types. To address these challenges, this study proposed a fully automatic flood detection framework (ATS-Flood) that integrates multi-temporal Sentinel-1 observations, adaptive thresholding, dual-polarization information, and post-processing refinement for accurate flood extent extraction. Unlike conventional approaches that rely on single-date SAR observations or empirical SAR indices, the proposed framework models the historical backscatter characteristics of each pixel using pre-flood Sentinel-1 time series and detects flooding based on statistically significant deviations from normal conditions. The integration of VV and VH polarizations, together with permanent-water and terrain-slope masks, effectively suppresses false alarms associated with topographic effects, permanent water bodies, and moisture-related backscatter variations. Furthermore, the proposed classification of flooded areas into SFS and WFS provides additional information beyond conventional binary flood maps, enabling a more comprehensive representation of flood severity and spatial distribution.

The framework was evaluated using the 2019 Khuzestan flood event and validated against Copernicus EMS reference data, Sentinel-2 imagery, and high-resolution optical observations. Quantitative assessment demonstrated an OA of 93.25%, a KC of 0.865, and F1-scores exceeding 93%, indicating a high level of agreement with the reference datasets. Sensitivity analyses further showed that the automatic Otsu threshold performs

785 comparably to manually optimized thresholds while providing superior automation and repeatability. In addition,
786 combining ascending and descending Sentinel-1 acquisitions consistently improved flood detection performance
787 compared with using either orbit independently, highlighting the benefit of exploiting complementary viewing
788 geometries. Comparative experiments with eight widely used flood mapping approaches, including S1-VV, S1-
789 VH, SDWI, NDFI-VV, NDFI-VH, UN-VV, UN-VH, and SBFD, confirmed the superiority of the proposed
790 framework. ATS-Flood achieved the highest accuracy across all evaluation metrics while producing more
791 spatially consistent flood maps and reducing both omission and commission errors. These improvements primarily
792 stem from the integration of temporal change analysis, automatic thresholding, and multi-polarization
793 information, which together enhance the robustness of flood detection under diverse environmental conditions.
794 The principal innovation of this study lies in modeling the historical backscatter behavior of each pixel using
795 multi-temporal pre-flood Sentinel-1 observations as a statistical baseline for flood detection. Rather than relying
796 on empirical backscatter thresholds or single-date SAR observations, the proposed framework identifies flooding
797 through statistically significant deviations from the historical behavior of each pixel. This strategy substantially
798 improves the robustness, transferability, and automation of flood mapping across diverse land-cover and
799 environmental conditions.

800 Although the proposed framework requires a sufficient archive of pre-flood Sentinel-1 observations and
801 currently relies exclusively on SAR imagery, these limitations do not compromise the validity of the presented
802 results. The comprehensive qualitative and quantitative evaluations, sensitivity analyses, and comparative
803 experiments consistently demonstrated that ATS-Flood provides accurate, robust, and reliable flood mapping,
804 making it suitable for large-scale operational applications. Given its high level of automation, computational
805 efficiency, and robust performance, ATS-Flood represents a promising solution for future operational flood
806 monitoring systems and near-real-time early warning services. Such capabilities could support disaster
807 management agencies by enabling rapid flood mapping and timely decision-making during emergency response
808 operations. Beyond its methodological contribution, the proposed framework also offers considerable practical
809 value for real-world flood management. Owing to its fully automated workflow, computational efficiency, and
810 high mapping accuracy, ATS-Flood has strong potential for integration into operational flood monitoring systems,
811 disaster management agencies, and near-real-time flood early warning services. Moreover, the generated flood
812 extent maps can provide valuable inputs for hydrological and hydraulic modeling, post-disaster damage
813 assessment, risk analysis, and evidence-based decision-making by emergency management authorities. Future
814 work will focus on integrating optical satellite observations, incorporating machine learning and deep learning

techniques, extending the framework to multi-sensor environments, and facilitating its implementation within operational flood monitoring and early warning systems for rapid disaster response.

Funding

This work is based upon research funded by Iran National Science Foundation (INSF) under project No 4040503.

Data Availability

Upon request, the corresponding author is willing to share the datasets analyzed in this research.

Acknowledgements

Authors would like to appreciate the Iran National Science Foundation (INSF) for partially supporting this research.

Disclosure Statements

No conflicts of interest or personal relationships are known to the authors that may have affected the work described in this article.

References

1- Amos, M. D., Okeke, F. N., Agbozu, E. N., Mogo, C. F., Ogidi, O. I., Eteh, D. R., Omonefe, F., Mogo, C. O., Winston, A. G., & Ihekona, O. (2026). Machine learning-based flood inundation mapping and LULC classification in Ahoada West, Rivers State, Nigeria using satellite imagery. *Discover Geoscience, 4*(1), 117.

2- Banerjee, A., & Daou, D. (2026). Explainable Flood Segmentation on Sentinel-1 SAR Imagery: A Comparative Study of CNN and Transformer Architectures. *arXiv preprint arXiv:2606.16302*.

3- Barkhade, V., Mahakarkar, S., Agrawal, R., Dhule, C., & Morris, N. C. (2023). *Flood extent mapping with unmanned aerial vehicles data using deep convolutional neural network.* Paper presented at the 2023 International Conference on Sustainable Computing and Smart Systems (ICSCSS).

4- Bayati, M., & Danesh-Yazdi, M. (2021). Mapping the spatiotemporal variability of salinity in the hypersaline Lake Urmia using Sentinel-2 and Landsat-8 imagery. *Journal of Hydrology, 595*, 126032.

5- Bereczky, M., Wieland, M., Krullikowski, C., Martinis, S., & Plank, S. (2022). Sentinel-1-based water and flood mapping: Benchmarking convolutional neural networks against an operational rule-based processing chain. *IEEE Journal of Selected Topics in Applied Earth Observations and Remote Sensing, 15*, 2023-2036.

6- Billah, M., Islam, A. S., Mamoon, W. B., & Rahman, M. R. (2023). Random forest classifications for landuse mapping to assess rapid flood damage using Sentinel-1 and Sentinel-2 data. *Remote Sensing Applications: Society and Environment, 30*, 100947.

7- Bioresita, F., Puissant, A., Stumpf, A., & Malet, J.-P. (2018). A method for automatic and rapid mapping of water surfaces from Sentinel-1 imagery. *Remote Sensing, 10*(2), 217.

8- Blaikie, P., Cannon, T., Davis, I., & Wisner, B. (2014). *At risk: natural hazards, people's vulnerability and disasters*: Routledge.

9- Canty, M. J., & Nielsen, A. A. (2017). *Spatio-temporal analysis of change with sentinel imagery on the Google Earth Engine.* Paper presented at the Proc. 2017 Conf. Big Data from Sp.
10- Change, I. P. O. C. (2001). Climate change 2007: Impacts, adaptation and vulnerability. *Genebra, Suíça*.
11- Chini, M., Hostache, R., Giustarini, L., & Matgen, P. (2017). A hierarchical split-based approach for parametric thresholding of SAR images: Flood inundation as a test case. *IEEE Transactions on Geoscience and Remote Sensing, 55*(12), 6975-6988.
12- Cian, F., Marconcini, M., & Ceccato, P. (2018). Normalized Difference Flood Index for rapid flood mapping: Taking advantage of EO big data. *Remote sensing of environment, 209*, 712-730.
13- Colomina, I., & Molina, P. (2014). Unmanned aerial systems for photogrammetry and remote sensing: A review. *ISPRS Journal of Photogrammetry and Remote Sensing, 92*, 79-97.
14- Dixit, A., & Chawla, I. (2026). Change map of flood detection using attention mechanism assisted quantum convolutional neural network utilising SAR and optical images. *International Journal of Image and Data Fusion, 17*(1), 2613394.
15- Dodangeh, P., Ebadi, H., & Kiani, A. (2021). Identification of flooded areas using time series statistical calculations and based on integrating radar and optical data. *Iranian journal of Ecohydrology, 8*(3), 623-639.
16- Du, Q., Li, G., Chen, D., Qi, S., Zhou, Y., Wang, F., & Cao, Y. (2023). Extracting water body data based on SDWI and threshold segmentation: A case study in permafrost area surrounding Salt Lake in Hoh Xil, Qinghai-Tibet Plateau, China. *Research in Cold and Arid Regions, 15*(4), 202-209.
17- Ebrahimi, E., Jamshidpour, N., & Homayouni, S. (2026). *Enhancing Flood Mapping Using Integrated SAR and Optical Image Fusion with U-Net++.* Paper presented at the 2026 IEEE Mediterranean and Middle-East Geoscience and Remote Sensing Symposium (M2GARSS).
18- Ezzine, A., Saidi, S., Hermassi, T., Kammessi, I., Darragi, F., & Rajhi, H. (2020). Flood mapping using hydraulic modeling and Sentinel-1 image: Case study of Medjerda Basin, northern Tunisia. *The Egyptian Journal of Remote Sensing and Space Science, 23*(3), 303-310.
19- Farhadi, H., Ebadi, H., Kiani, A., & Asgary, A. (2024a). Near Real-Time Flood Monitoring Using Multi-Sensor Optical Imagery and Machine Learning by GEE: An Automatic Feature-Based Multi-Class Classification Approach. *Remote Sensing, 16*(23), 4454.
20- Farhadi, H., Ebadi, H., Kiani, A., & Asgary, A. (2024b). A novel flood/water extraction index (FWEI) for identifying water and flooded areas using sentinel-2 visible and near-infrared spectral bands. *Stochastic Environmental Research and Risk Assessment, 38*(5), 1873-1895.
21- Farhadi, H., Ebadi, H., Kiani, A., & Asgary, A. (2025a). Introducing a new index for flood mapping using Sentinel-2 imagery (SFMI). *Computers & Geosciences, 194*, 105742.
22- Farhadi, H., Esmaeily, A., & Najafzadeh, M. (2022). Flood monitoring by integration of Remote Sensing technique and Multi-Criteria Decision Making method. *Computers & Geosciences, 160*, 105045.
23- Farhadi, H., Kiani, A., Ebadi, H., & Asgary, A. (2025b). Development of an automatic time-series flood mapping framework using Sentinel-1 and 2 imagery. *Stochastic Environmental Research and Risk Assessment*, 1-29.
24- Farhadi, H., & Najafzadeh, M. (2021). Flood risk mapping by remote sensing data and random forest technique. *Water, 13*(21), 3115.
25- Feyisa, G. L., Meilby, H., Fensholt, R., & Proud, S. R. (2014). Automated Water Extraction Index: A new technique for surface water mapping using Landsat imagery. *Remote sensing of environment, 140*, 23-35.
26- Gao, B.-C. (1996). NDWI—A normalized difference water index for remote sensing of vegetation liquid water from space. *Remote sensing of environment, 58*(3), 257-266.
27- Garg, S., Dasgupta, A., Motagh, M., Martinis, S., Borgomeo, E., & Selvakumaran, S. (2025). *Improving flood detection in Arid regions using Sentinel-1 Interferometric Coherence and Machine learning.* Paper presented at the ESA Living Planet Symposium 2025.
28- Gašparović, M., & Klobučar, D. (2021). Mapping floods in lowland forest using sentinel-1 and sentinel-2 data and an object-based approach. *Forests, 12*(5), 553.

29- Giordan, D., Hayakawa, Y., Nex, F., Remondino, F., & Tarolli, P. (2018). The use of remotely piloted aircraft systems (RPASs) for natural hazards monitoring and management. *Natural Hazards and Earth System Sciences, 18*(4), 1079-1096.
30- Hosseiny, B., Ghasemian, N., & Amini, J. (2019). A convolutional neural network for flood mapping using sentinel-1 and Srtm Dem data: case study in Poldokhtar-Iran. *The International Archives of the Photogrammetry, Remote Sensing and Spatial Information Sciences, 42*, 527-533.
31- Hotaki, S., Motagh, M., & Haghighi, M. (2025). *Enhanced Flood Mapping Through Coherent and Incoherent Change Detection: A Sentinel-1 SAR Time-Series Analysis.* Paper presented at the AGU Fall Meeting Abstracts.
32- Hotaki, S. F., Haghighi, M. H., & Motagh, M. (2026). Coherent and incoherent change detection for improved flood mapping: A Sentinel-1 SAR time-series approach. *Remote Sensing Applications: Society and Environment*, 101961.
33- Kaçmaz, A., & Alganci, U. (2026). SAR-Based Flood Extent Mapping with a Lightweight Siamese U-Net and Differential Attention Mechanism. *Earth, 7*(3), 87.
34- Lan, L., & Wang, X. (2025). Large-scale flood mapping using Sentinel-1 and Sentinel-2 imagery: Spatio-temporal analysis of the 23· 7 Haihe basin-wide extreme flood. *Journal of Hydrology, 653*, 132777.
35- Landuyt, L., Van Wesemael, A., Van Coillie, F., & Verhoest, N. E. (2018). *SAR-based flood mapping: an assessment of established approaches.* Paper presented at the EGU General Assembly Conference Abstracts.
36- Lee, J.-S., Wen, J.-H., Ainsworth, T. L., Chen, K.-S., & Chen, A. J. (2008). Improved sigma filter for speckle filtering of SAR imagery. *IEEE Transactions on Geoscience and Remote Sensing, 47*(1), 202-213.
37- Li, C., Dash, J., Asamoah, M., Sheffield, J., Dzodzomenyo, M., Gebrechorkos, S. H., Anghileri, D., & Wright, J. (2022). Increased flooded area and exposure in the White Volta river basin in Western Africa, identified from multi-source remote sensing data. *Scientific Reports, 12*(1), 3701.
38- Li, S., Liu, K., & Wang, Q. (2026). Near-real-time SAR flood detection using feature fusion and region-adaptive deep learning method. *Journal of Hydrology*, 135523.
39- Li, Y., Martinis, S., Plank, S., & Ludwig, R. (2018). An automatic change detection approach for rapid flood mapping in Sentinel-1 SAR data. *International Journal of Applied Earth Observation and Geoinformation, 73*, 123-135.
40- Li, Z., Li, R., Zhang, Z., & Tian, F. (2025). Flood mapping in SAR images via threshold segmentation with hydrological-hydrodynamic modeling. *Journal of Hydrology*, 134825.
41- Liang, J., & Liu, D. (2020). A local thresholding approach to flood water delineation using Sentinel-1 SAR imagery. *ISPRS Journal of Photogrammetry and Remote Sensing, 159*, 53-62.
42- Martinis, S., Kersten, J., & Twele, A. (2015). A fully automated TerraSAR-X based flood service. *ISPRS Journal of Photogrammetry and Remote Sensing, 104*, 203-212.
43- Martinis, S., Twele, A., & Voigt, S. (2009). Towards operational near real-time flood detection using a split-based automatic thresholding procedure on high resolution TerraSAR-X data. *Natural Hazards and Earth System Sciences, 9*(2), 303-314.
44- McFeeters, S. K. (1996). The use of the Normalized Difference Water Index (NDWI) in the delineation of open water features. *International Journal of Remote Sensing, 17*(7), 1425-1432.
45- Moharrami, M., Javanbakht, M., & Attarchi, S. (2021). Automatic flood detection using sentinel-1 images on the google earth engine. *Environmental monitoring and assessment, 193*(5), 248.
46- Mohsenifar, A., Mohammadzadeh, A., & Jamali, S. (2025). Unsupervised Rural Flood Mapping from Bi-Temporal Sentinel-1 Images Using an Improved Wavelet-Fusion Flood-Change Index (IWFCI) and an Uncertainty-Sensitive Markov Random Field (USMRF) Model. *Remote Sensing, 17*(6), 1024.
47- Mosalla Tabari, M., Ebadi, H., & Alizadeh Zakaria, Z. (2025). PSO-random forest approach to enhance flood-prone area identification: using ground and remote sensing data (case study: Ottawa-Gatineau). *Earth Science Informatics, 18*(2), 215.
48- Otsu, N. (1979). A threshold selection method from gray-level histograms. *Automatica, 11*(285-296).

49- Pekel, J.-F., Cottam, A., Gorelick, N., & Belward, A. S. (2016). High-resolution mapping of global surface water and its long-term changes. *Nature, 540*(7633), 418-422. doi:10.1038/nature20584
50- Pulvirenti, L., Chini, M., Pierdicca, N., Guerriero, L., & Ferrazzoli, P. (2011). Flood monitoring using multi-temporal COSMO-SkyMed data: Image segmentation and signature interpretation. *Remote sensing of environment, 115*(4), 990-1002.
51- Risling, A., Lindersson, S., & Brandimarte, L. (2024). A comparison of global flood models using Sentinel-1 and a change detection approach. *Natural Hazards, 120*(12), 11133-11152.
52- Schlaffer, S., Matgen, P., Hollaus, M., & Wagner, W. (2015). Flood detection from multi-temporal SAR data using harmonic analysis and change detection. *International Journal of Applied Earth Observation and Geoinformation, 38*, 15-24.
53- Schumann, G. J.-P., & Moller, D. K. (2015). Microwave remote sensing of flood inundation. *Physics and Chemistry of the Earth, Parts a/b/c, 83*, 84-95.
54- Schumann, G. J., Brakenridge, G. R., Kettner, A. J., Kashif, R., & Niebuhr, E. (2018). Assisting flood disaster response with earth observation data and products: A critical assessment. *Remote Sensing, 10*(8), 1230.
55- Seydi, S. T., Saeidi, V., Kalantar, B., Ueda, N., van Genderen, J. L., Maskouni, F. H., & Aria, F. A. (2022). Fusion of the multisource datasets for flood extent mapping based on ensemble convolutional neural network (CNN) model. *Journal of Sensors, 2022*(1), 2887502.
56- Tellman, B., Sullivan, J. A., Kuhn, C., Kettner, A. J., Doyle, C. S., Brakenridge, G. R., Erickson, T. A., & Slayback, D. A. (2021). Satellite imaging reveals increased proportion of population exposed to floods. *Nature, 596*(7870), 80-86.
57- Tripathy, P., & Malladi, T. (2022). Global Flood Mapper: a novel Google Earth Engine application for rapid flood mapping using Sentinel-1 SAR. *Natural Hazards, 114*(2), 1341-1363.
58- Twele, A., Cao, W., Plank, S., & Martinis, S. (2016). Sentinel-1-based flood mapping: a fully automated processing chain. *International Journal of Remote Sensing, 37*(13), 2990-3004.
59- UN-SPIDER. (2021). Recommended practice: flood mapping and damage assessment using Sentinel-1 SAR data in google earth engine. *In: UN-SPIDER knowledge portal.* doi:https://un-spider.org/advisory-support/recommended-practices/recommended-practice-google-earth-engine-flood-mapping
60- Xu, H. (2006). Modification of normalised difference water index (NDWI) to enhance open water features in remotely sensed imagery. *International Journal of Remote Sensing, 27*(14), 3025-3033.
61- Yu, H., Xu, Y.-P., Huang, Y., & Chiang, Y.-M. (2026). Flood inundation monitoring with multi-source satellite imagery based on deep learning and explainable frameworks. *Journal of Hydrology*, 135409.